Photothermal Depletion of Cancer-Associated Fibroblasts Normalizes Tumor Stiffness in Desmoplastic Cholangiocarcinoma

Alba Nicolás-Boluda, Javier Vaquero, Gautier Laurent, Gilles Renault, Rana Bazzi, Emmanuel Donnadieu, Stéphane Roux, Laura Fouassier, Florence Gazeau

Photothermal Depletion of Cancer-Associated Fibroblasts Normalizes Tumor Stiffness in Desmoplastic Cholangiocarcinoma

*Alba Nicolás-Boluda[1,2], Javier Vaquero[3], Gautier Laurent[4], Gilles Renault[2], Rana Bazzi[4], Emmanuel Donnadieu[2], Stéphane Roux[4], Laura Fouassier[3]†, Florence Gazeau[1]†**

1. Laboratoire Matière et Systèmes Complexes (MSC), Université de Paris, CNRS-UMR 7057, Paris, 75013, France

2. Institut Cochin, Université de Paris, INSERM U1016/CNRS UMR 8104, Paris, 75014, France

3. Sorbonne Université, INSERM, Centre de Recherche Saint-Antoine, CRSA, Paris, 75012, France

4.Institut UTINAM, CNRS UMR 6213, Université Bourgogne Franche-Comté, Besançon, 25010, France

* Corresponding author: florence.gazeau@univ-paris-diderot.fr

† These authors contributed equally.

Abstract

Physical oncology recognizes tissue stiffness mediated by activation of cancer-associated fibroblasts (CAF) and extracellular matrix (ECM) remodeling as an active modulator of tumorigenesis, treatment resistance and clinical outcome. Cholangiocarcinoma (CCA) is a highly aggressive and chemoresistant desmoplastic cancer enriched in CAF. CCA's stroma mechanical properties are considered responsible for its chemoresistant character. To normalize tumor mechanics, we propose a physical strategy based on remotely light activated nanohyperthermia to modulate the tumor micro-environment. In this study, we report the use of multifunctional iron oxide nanoflowers decorated with gold nanoparticles (GIONF) as efficient nanoheaters to achieve complete tumor regression following three sessions of mild-hyperthermia. The preferential uptake of GIONF by CAF allowed targeting this cell population, which resulted in a significant early reduction of tumor stiffness followed by tumor regression. In conclusion, our study highlights a spatially and temporally controlled physical strategy, GIONF-mediated photothermal therapy, to deplete CAF and normalize the tumor mechanics that may apply to desmoplastic cancer and CCA treatment.

Keywords

photothermal therapy, cancer-associated fibroblast, cholangiocarcinoma, iron oxide nanoflowers, stiffness

Cholangiocarcinoma (CCA) is a biliary tract cancer that is classified based on its location within the bile ducts: intrahepatic, perihilar and distal CCA. CCAs represent the second most frequent type of primary liver cancer and ~3% of all gastrointestinal neoplasia.[1] The incidence of intrahepatic CCA has increased drastically over the past years although the causal factors are not clearly identified yet. The overall prognosis is very poor due to its late diagnosis and the development of resistance to chemotherapies.[1] The only therapeutic option, surgical resection, is often compromised representing only 20% of cases. After curative surgery, 5-year survival rate of CCA patients varies among 15-40%. When surgery cannot be performed, patients undergo palliative chemotherapy with a combination of gemcitabine and platinum salt, the reference chemotherapy validated for advanced unresectable CCA.[2] In case of tumor progression after this first line of treatment, there is no other treatment approved. For this reason, the development of new therapies for CCA is of upmost importance.

CCA is characterized by a desmoplastic stroma and an abundant tumor extracellular matrix (ECM). At the cellular level, the cellular microenvironment of CCA is abundantly formed of cancer-associated fibroblasts (CAF), suggesting a fundamental role of these cells in tumor growth and progression, which has been confirmed by several studies. A strong expression of α-SMA, a marker of CAF, is observed in 50% of CCA tumors and is associated with poor prognosis. Studies have illustrated the major role played by the CAF in CCA progression, and several signaling pathways involved in the reciprocal communication between CAF and tumor cells have been reported.[3] Among them, a major pathway, the transforming growth factor β (TGFβ) is deregulated in the tumor microenvironment (TME) of poor prognosis CCA.[4]

The physical properties of the tumor microenvironment (TME) comprising ECM and stromal cells have demonstrated to have important clinical implications in the course of tumor progression

and resistance to chemotherapy. Solid tumors are characterized by a reduced and heterogeneous blood supply due to defective and dysfunctional vasculature, restricting therapeutic drug delivery into the tumor.[5] ECM mechanics has also been shown to play an important role in chemoprotection.[6] The fibrosis and progressive stiffening in many solid desmoplastic tumors such as CCA, are mainly due to excessive accumulation and linearization of collagen fibers that form a physical barrier particularly difficult to penetrate. The high deposition of collagen around the tumor islet increases the resistance to interstitial flow within the tumor leading to an increase of interstitial pressure. High interstitial pressure blocks the diffusion of small molecules within the tumor, including therapeutic molecules, leaving them concentrated in perivascular regions. This phenomenon has also been observed with therapeutic antibodies.[7] Considering all this, the use of TME-targeted strategies as adjuvants to chemotherapy, may improve CCA therapy. Given that the abundance of CAF in CCA stroma is critical for tumor development and associated with poor prognosis[3] CAF represent an attractive target of TME to envision new therapies for CCA. CAF produce a variety of cytokines and growth factors such as TGFβ, vascular endothelial growth factor (VEGF), platelet-derived growth factor (PDGF), heparin-binding EGF-like growth factor (HB-EGF).[3] They secrete also ECM components, in particular fibrillary collagen and fibronectin, which, as aforementioned form a physical barrier against drug penetration [8] but are also responsible for tumor stiffening. In fact, the correlation between tumor stiffness and the response to neoadjuvant chemotherapy shows that compliant tumors are more responsive than stiff tumors.[9] It is therefore evident that targeting the TME and in particular tumor ECM through CAF modification or depletion could be an attractive therapeutic option for CCA. Indeed, tentative treatment of CCA by depleting CAF has been previously tested and gave encouraging data.[10]

Physical therapies, based on the use of electromagnetic or acoustic waves (such as high-intensity focused ultrasound (HIFU) or spatially controlled nanoparticle-mediated magnetic hyperthermia or photothermal therapy (PTT)), have been intensely studied in the last decade. They represent an

adjuvant or neo-adjuvant strategy to be applied in chemoresistant tumors such as CCA. The main principle in these therapies is the use of nanoparticles that can remotely be activated by an external stimulus such as a laser or an alternating magnetic field, generating a controlled hyperthermia in the target region. In particular, PTT is a minimally invasive hyperthermia treatment based on the conversion of optical energy into thermal energy by nanoparticles upon near-infrared laser irradiation. There currently exist a large panel of photoactivable nanomaterials including plasmonic metallic nanoparticles (*i.e.* gold nanoparticles or nanostars),[11,12] carbon absorbing nanomaterials (*i.e.* carbon nanotubes) or iron oxide nanoparticles.[13] In order to select appropriate nanomaterial as a PTT agent, in addition to its absorption cross-section for optical wavelength, other parameters must be considered such as low toxicity, easy to functionalize and scale-up, and favorable biodistribution, biodegradation, and life cycle *in vivo*.[14] In addition, the design of multimodal nanoparticles is of upmost interest for the combination of multiple therapeutic and diagnostic techniques. Hybrid composite nanostructures made from the combination of plasmonic metals and magnetic iron oxide are particularly interesting due to their multifunctional properties ranging from imaging and diagnosis to therapeutics.[15] Iron oxide nanoflower-like monocrystalline nanoparticles (IONF) have previously been reported for their outstanding cooperative magnetic properties,[16,17] which make them excellent nanoheaters under alternating magnetic field and MRI contrast agent. Moreover, a controlled biodegradability of iron oxide nanoflowers has been reported in cellular environment. [18] Iron oxide nanoparticles benefit from being processed by the finely regulated iron metabolism, which allows recycling of released iron by endogeneous ferritin while minimize toxicity.[19] On the other hand, ultrasmall 2-3 nm gold nanoparticles have been proposed as radiosensitizing nanoagents to enhance the efficacy and local control of radiotherapy, while allowing image-guided therapy and fast renal clearance.[20] We discovered recently that such tiny gold nanoparticles can be safely degraded by cell lysosomes, much faster than larger particles, involving gold metabolization by metallothioneins.[21]

Since the *in vivo* behavior of the ultrasmall nanoparticles is safer than the one of larger gold nanoparticles, the potential of ultrasmall nanoparticles for PTT deserves to be exploited. For this reason, we propose to graft ultrasmall radiosensitizing Au@DTDTPA nanoparticles onto large and biodegradable IONF. This strategy aims to provide efficient nanoheaters for PTT that can be metabolized. It also leads to the development of hybrid nanostructures for combinatory therapies including radiosensitization, magnetic hyperthermia and PTT as well as multimodal imaging. In this study, we evaluate the design of such iron oxide nanoflower-like multicore nanoparticle (IONF) decorated with ultrasmall 2-3 nm gold nanoparticles (Au@DTDTPA) (GIONF) to substantially enhance their heating efficiency under NIR light irradiation compared to the non-decorated ones and achieve therapeutic PTT in a prototypical desmoplastic tumor.

Although PTT has been proposed in many preclinical studies and is under development in clinical trials, there are multiple targets of nanoparticle-mediated hyperthermia in TME. The various and multiscale outcomes of PTT are still challenging to decipher because they strongly depend on tumor structure and heterogeneity as well as nanoparticle properties that can determine their affinity for ECM components or cell types susceptible to internalize them.[22] A crucial parameter to consider is the nanoparticle fate within the TME, since the biological outcome of localized heating will highly depend on their localization. Here we decipher the interactions of IONF/GIONF with the different cellular and matrix components of TME and highlight the respective outcome of PTT treatment. This approach was done on a co-culture model of fibroblasts and tumor cells, sheep tendon to assess the effects on collagen fibers, and *in vivo* in CCA tumor in mice with a longitudinal monitoring of tumor stiffness by shear wave elastrography (SWE). By demonstrating the differential uptake of GIONF uptake in the different cell types of TME, we highlight their preferential accumulation by CAFs, which allowed the performance of a targeted PTT in the stromal compartment, leading to CAF depletion, tumor softening and finally tumor regression.

Results/Discussion

Gold Decorated Iron Oxide Nanoflowers (GIONF) Exhibit Higher Heating Capacity than Iron Oxide Nanoflowers (IONF) in Solution Exposed to a NIR Laser

IONF are small isotropic assemblies of small nanocrystalline iron oxide nanoparticles of approximately 11 nm that are assembled in a flower-resembling monocrystalline structure whose size can range between 25-30 nm (Figure 1A).[16] Ultrasmall gold nanoparticles, composed of a gold core (2-3 nm) coated with dithiolated diethylenetriaminepentaacetic acid (Au@DTDTPA) can be immobilized onto large IONF resulting in GIONF. The coupling of Au@DTDTPA onto IONF does not affect IONF size (Figure 1A). Au@DTDTPA, due to their small gold core size (2-3 nm) are not easily visible by transmission electron microscopy (TEM). However, using high-angle annular dark-field imaging (HAADF), it is easier to distinguish the gold nanoparticles on the IONFs (white spots, Figure 1B). The mean number of Au@DTDTPA per IONF has been estimated to be between 28 (for the smallest IONFs) and 49 (for the largest one) based on the ICP-AES quantification of iron and gold and taking into account the volumetric mass density of gold metal and of maghemite and the core radius of each type of nanoparticles. These hybrid nanostructures have been previously designed in order to maximize the tumor retention of Au nanoparticles and to prolong the radiosensitization effects locally in the tumor since Au@DTDTPA alone suffer from premature renal clearance.[23]

IONF present outstanding magnetic properties that are of great interest for T_2-weighted magnetic resonance imaging (MRI), magnetic targeting and alternating magnetic field hyperthermia.[17] They are also characterized by their gradual degradation that can be modulated by modifying their coating.[18] On the other side, Au@DTDTPA is capable of forming stable complexes with metal ions, allowing easy functionalization with imaging agents such as ^{99m}Tc or gadolinium and use for image-guided radiosensitization.[20] The combination of both nano-objects results in the merge of their properties in a

single nanostructure. GIONF are, therefore, capable of acting as a multimodal imaging agent for both MRI and other imaging techniques such as single photon emission computed tomography (SPECT), depending on the ions entrapped in the organic shell of the Au@DTDTPA. In order to complete the potential of using GIONF as theranostic agents, we evaluated the efficiency of GIONF and IONF as photothermal agents for PTT.

The heating efficiencies of IONF and GIONF in colloidal suspension were compared at two different iron concentrations (1 mg/mL and 100 μg/mL) when submitted to a NIR irradiation (808 nm) at 2.2 W/cm^2. The surface temperature of the suspension was recorded with an infrared camera. The heating efficiency was evaluated by calculating the temperature increase (ΔT) of the solution as well as the concentration-normalized specific absorption rate (SAR) (Figures 1C-1E).

At both concentrations, the ΔT of IONF was lower than the one of GIONF, the difference being more significant at 1 mg/mL (Figures 1D and 1E). The SAR at 100 μg/mL of both solutions was not significantly different (GIONF = 3455 *vs* IONF= 3934 W/g), whilst at 1mg/mL the SAR of GIONF was nearly double that of IONF (GIONF = 2529 *vs* IONF = 1395 W/g) (Figure 1E). NIR PTT effect is correlated with the optical absorption of the nanomaterial in the NIR region. As already observed in other types of iron oxide nanoparticles,[24,25] iron oxide nanoflowers exhibit an extended optical absorbance that gradually decreases from the UV to the NIR region (Figures S1A and S1C). When zooming into the NIR region we can see that GIONF have a slightly higher absorbance than IONF (Figures S1B and S1D). This difference was only observed at 1mg/mL and not at 100μg/mL.

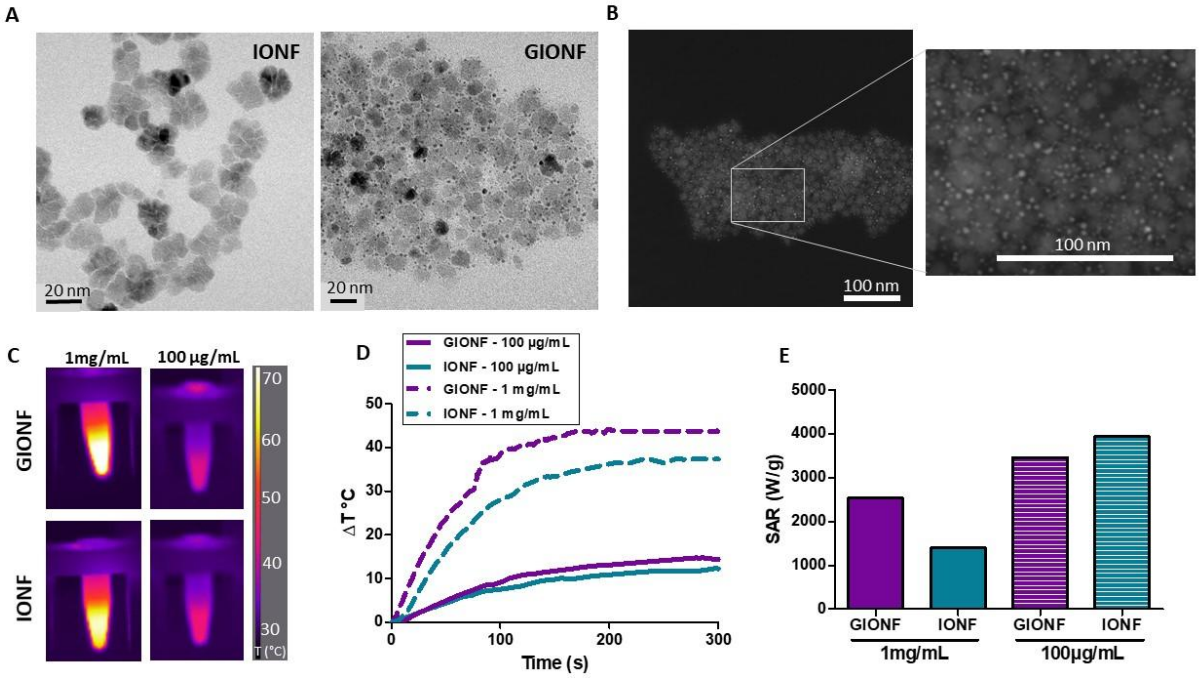

Figure 1. IONF and GIONF heating efficiency. A) TEM images of GIONF and IONF. Scale bar = 20 nm. B) STEM-HAADF images of GIONF. Scale bar = 100 nm. C) Infrared thermal images of the IONF and GIONF aqueous dispersions (100 µL) after 5 min of 808 nm laser irradiation. D) Temperature increase of IONF and GIONF aqueous solutions ([Fe] =1mg/mL and 100 µg/mL) upon irradiation with an 808 nm laser (2.2 W/cm^2). E) Specific absorption rate (SAR) of IONF and GIONF.

GIONF Heating Capacity is still Higher when Internalized in Tumor Cells

Previous studies have shown that within a biological environment and especially when internalized by cells nanoparticles can undergo physico-chemical modifications as well as different degrees of aggregation due to lysosomal confinement.[26] This can directly affect their photothermal efficiency. Hence, beyond validating the advantage of GIONF *versus* IONF in terms of heating efficiency in

solution, it is important to compare those two nanoformulations when internalized in cells. To do so, GIONF and IONF were incubated with human cholangiocarcinoma cell line, EGI-1, for 24 hours at a concentration of [Fe]=112µg/mL (Figure 2A). Cells were washed to discard the excess of nanoparticles not internalized by cells. One million GIONF and IONF-loaded EGI-1 cells were pelleted and resuspended in a small volume (100µL) for PTT experiments. The experimental setup was the same as for the nanoparticles in solution (808 nm irradiation at 2.2 W/cm^2 for 5 minutes) (Figure 2A). Importantly, GIONF heating efficiency remained higher than that of IONF when internalized in EGI-1 tumor cells. The difference of laser-induced temperature increment, ΔT, generated by gold decorated nanoflowers (GIONF) in comparison to the raw nanoflowers (IONF) internalized by EGI-1 tumor cells is 5°C. The maximal temperature reached by GIONF-loaded EGI-1 tumor cells is 50.8 °C, whilst that of IONF-loaded cells is 45.6°C. In order to normalize the measurements and to investigate if the difference in heating efficiency was related to a different cellular uptake, the concentration of iron reflecting the amount of nanoparticles internalized in cells was quantified by Inductively Coupled Plasma – Atomic Emission Spectroscopy (ICP-AES) after 24 hours incubation with [Fe]=112, 56 and 11 µg/mL of IONF or GIONF. Results show that both IONF and GIONF are up taken in a dose-dependent manner without cytotoxicity (Figure S2A), but surprisingly IONF are more internalized than GIONF in cholangiocarcinoma cells, EGI-1 (Figure 2D). The lower uptake of gold-decorated nanoflowers in tumor cells may be partly attributed to the highly hydrophilic nature of Au@DTDTPA which enhances the hydrophilicity of IONF and confer negative charges to the GIONF hybrid structures at physiological pH. Upon 24 h internalization in cells, both IONF and GIONF are localized and confined in endo-lysosomal compartments (Figures 2E). Interestingly, the Au@DTDTPA appear to have dissociated from the IONF in cell lysosome since we identify Au@DTDTPA clusters in the endosomes together with bare IONF (Figure 2E, orange circle). The gold/iron proportion of original

nanohybrids was, therefore, not maintained upon GIONF internalization in cells. Measurements performed with ICP that allowed quantifying the amount of gold and iron in cells showed that the gold/iron concentration ratio is slightly lower in cells in comparison to the stock solution by a factor of 1.2 in average (Figure S4), suggesting early dissociation in culture medium or on contact with cells and differential cell uptake. It must be emphasized that despite the loss of Au@DTDTPA decoration in cells, GIONF heated more the cells than IONF although they were internalized to a lesser extent. This effect could be quantified by calculating the Specific absorption rate (SAR) in cells. The SAR of GIONF internalized in EGI-1 cells was 4581 W/g, whilst that of IONF was 2940 W/g (Figure 2F). This means that intracellular confinement is beneficial to the heating capacity of GIONF, presumably because Au@DTDTPA that have dissociated from the GIONF structure are brought nearer to each other as clusters, favoring plasmon coupling between the ultrasmall gold particles which can shift to NIR region their optical absorption.

To test the biocompatibility of IONF and GIONF, we next tested their cytotoxicity in 4 different cell lines: the human cholangiocarcinoma cell line (EGI-1) and three non-tumoral cell lines including immortalized human liver stellate fibroblasts (hTERT-HSC), human endothelial cells (HUVEC) and murine macrophage (RAW 264.7). Results show that both IONF and GIONF are not cytotoxic after 24 hrs incubation in the concentration range [Fe]=10-100 µg/mL (Figure S2A-D). However, at very high concentrations ([Fe] = 100-500 µg/mL) viability level are less than 70% for both HUVEC and hTERT cells (Figure S2B and S2D). Hemolysis studies have also been performed to test the biocompatibility of both IONF and GIONF in red blood cells (Figure S3). The level of hemolysis was not significantly enhanced in comparison to the control for IONF or GIONF concentration from 50 to 1000 µg/mL. Overall these results confirm the *in vitro* safety in the use of both IONF and GIONF.

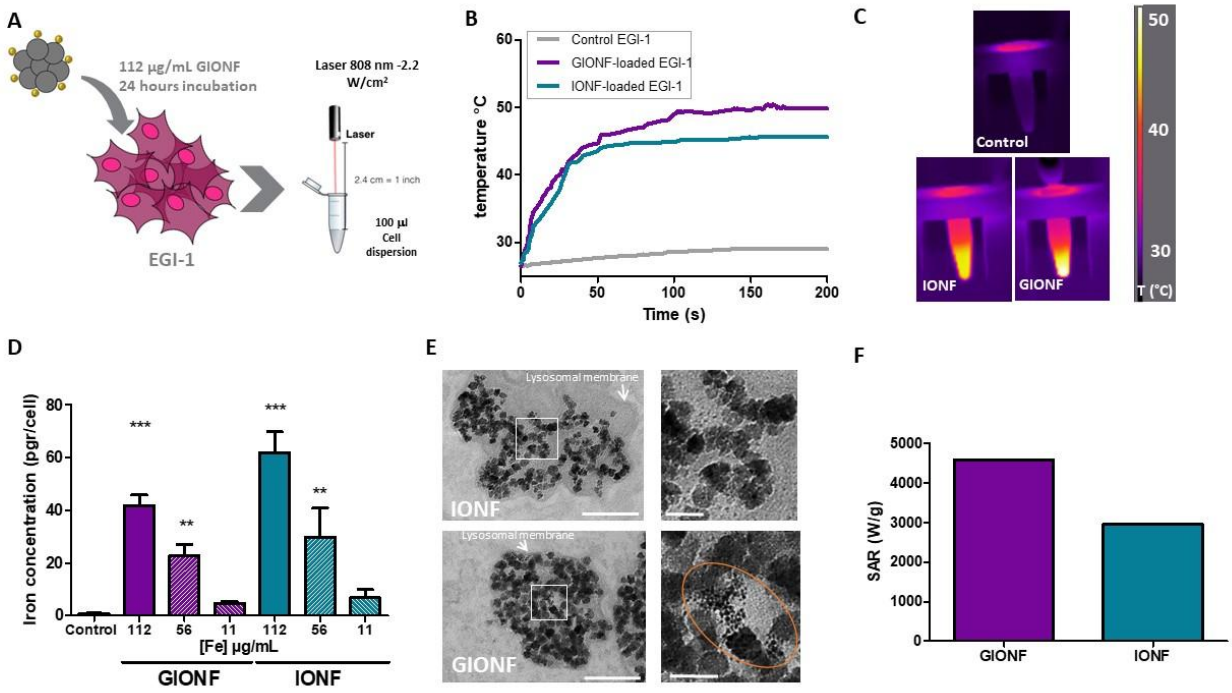

Figure 2. IONF and GIONF heating capacity in cells. A) Illustrative schema of the experimental setup. B) Temperature increase of IONF and GIONF internalized in EGI-1 cells upon irradiation with an 808 nm laser (2.2 W/cm^2). C) Infrared thermal images of IONF and GIONF internalized in EGI-1 cells, dispersed in 100 µL of PBS after 5 min of 808 nm laser irradiation. D) Quantification of iron in EGI-1 when incubated with GIONF and IONF at different concentrations: 112, 56 and 11 µg/mL. E) TEM images of EGI-1 cells after 24-hour incubation with IONF and GIONF. Au@DTDTPA clusters present in the endosomes are indicated by the orange circle. Scale bar = 200 nm. Zoom in scale bar = 50 nm. F) SAR of GIONF and IONF internalized in EGI-1 cells.

GIONF Uptake by Stromal Cells Indicate a Preferential Targeting of Fibroblasts

Since cells of the TME have a major influence on tumor progression and therapeutic response,[6] we decided to investigate the interaction between GIONF and stromal cells. For that, we studied the internalization of both IONF and GIONF in two of the most abundant cells in the stroma: fibroblasts

and macrophages. hTERT-HSC and RAW 264.7 as a model of fibroblasts and of macrophages, respectively, were incubated with IONF and GIONF at three different concentrations ([Fe] = 112, 56, 11.2 μg/mL). Unlike to what has been previously observed in EGI-1 cholangiocarcinoma cells, GIONF were internalized twice as much as IONF in both fibroblasts and macrophages (Figures 3A and 3B). In addition, GIONF internalization was 5 times higher in fibroblasts than in macrophages and 10 times higher than in EGI-1 cells. In order to test the competitive uptake of GIONF between fibroblasts and tumor cells, we performed uptake experiments in a co-culture model. For that, EGI-1 (mCherry) and hTERT (GFP) cells were co-cultured in a ratio 1:1 and were left to grow for 5-7 days. The resulting co-culture reproduces the stromal architecture seen in CCA tumors: tumor cells forming islets surrounded by abundant stroma composed by fibroblasts. GIONF and IONF were incubated overnight with the co-cultures and after washing-off the non-internalized left over nanoparticles, the cocultures were imaged using a confocal microscope (Figure 3C). The ratio of nanoparticles internalized in tumor cells or in fibroblasts was quantified using brightfield images, as nanoparticles accumulated into lysosomes are easily seen as dark spots. Results indicate that fibroblasts internalized better GIONF and IONF compared to tumor cells even in a competitive environment, confirming preferential targeting of fibroblasts for both nanoparticles (Figure 3D).

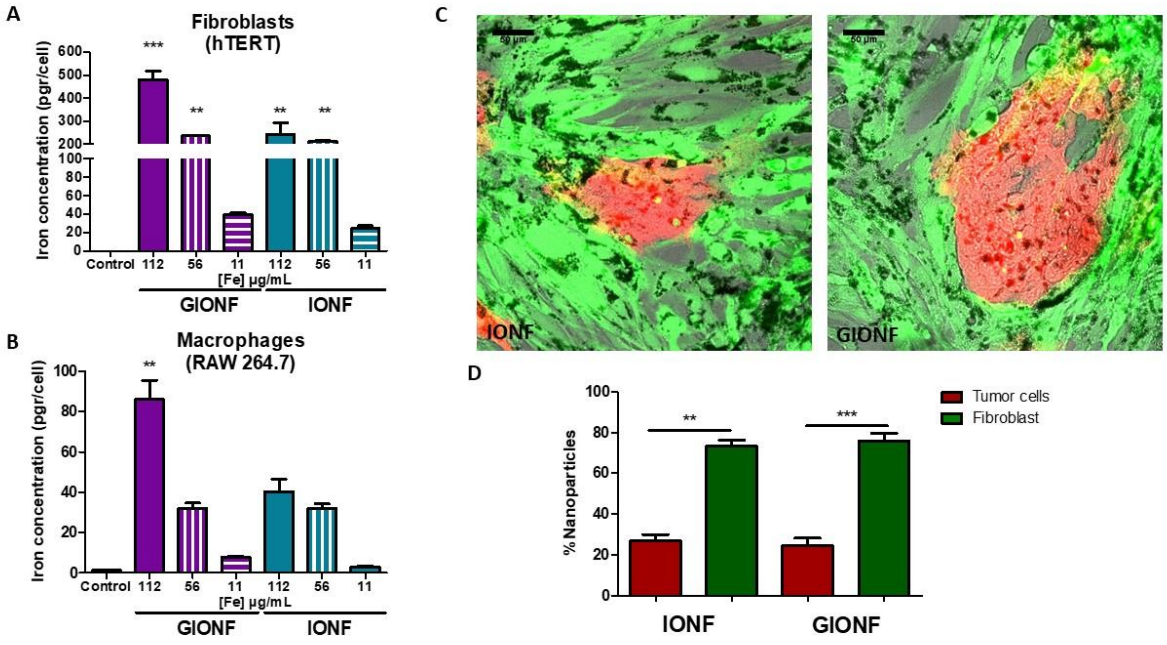

Figure 3. Preferential uptake of GIONF by fibroblasts. Quantification of iron in A) hTERT-HSC fibroblasts (hTERT-HSC) and B) in macrophages (RAW264.7) when incubated with GIONF and IONF at different concentrations: [Fe] 112, 56 and 11 µg/mL. C) Confocal microscopy image of hTERT-HSC:EGI-1 cocultures incubated with [Fe] 112 µg/mL GIONF and IONF. hTERT-HSC cells are identified in green (GFP), whilst EGI-1 tumor cells are labelled in red (mCherry), both GIONF and IONF can be easily identified as black spots inside the cells. Scale bar = 50 µm. D) Quantification of the percentage of nanoparticles located in fibroblast and in tumor cells in hTERT-HSC:EGI-1 cocultures.

We were also interested in checking whether the irradiation of these 2D confluent co-cultures using a near-infrared laser, would allow the destructuration of the co-culture, meaning that nanoparticle-containing cells were probably killed during the irradiation. As seen on Figure 4A, upon 808 nm direct laser irradiation for 10 min at 1W/cm^2 around 10% of the co-culture surface was destroyed, meaning that cell death has been induced and dead cells were probably detached and lost during the washing

steps. There was not a significant difference between the percentage of co-culture damaged after IONF- or GIONF-mediated PTT (Figure 4B). In order to evaluate cell death produced by GIONF/IONF-mediated PTT, cell necrosis and apoptosis were evaluated. Results showed higher proportion of cell death by apoptosis than by necrosis (Figure 4C), however we cannot rule out the fact that cells in late-necrosis stage may have already been detached, being responsible for the observed destructuration of the co-cultures. Higher levels of cell death have been observed in the cocultures during GIONF-mediated PTT, however the difference with IONF was not statistically significant

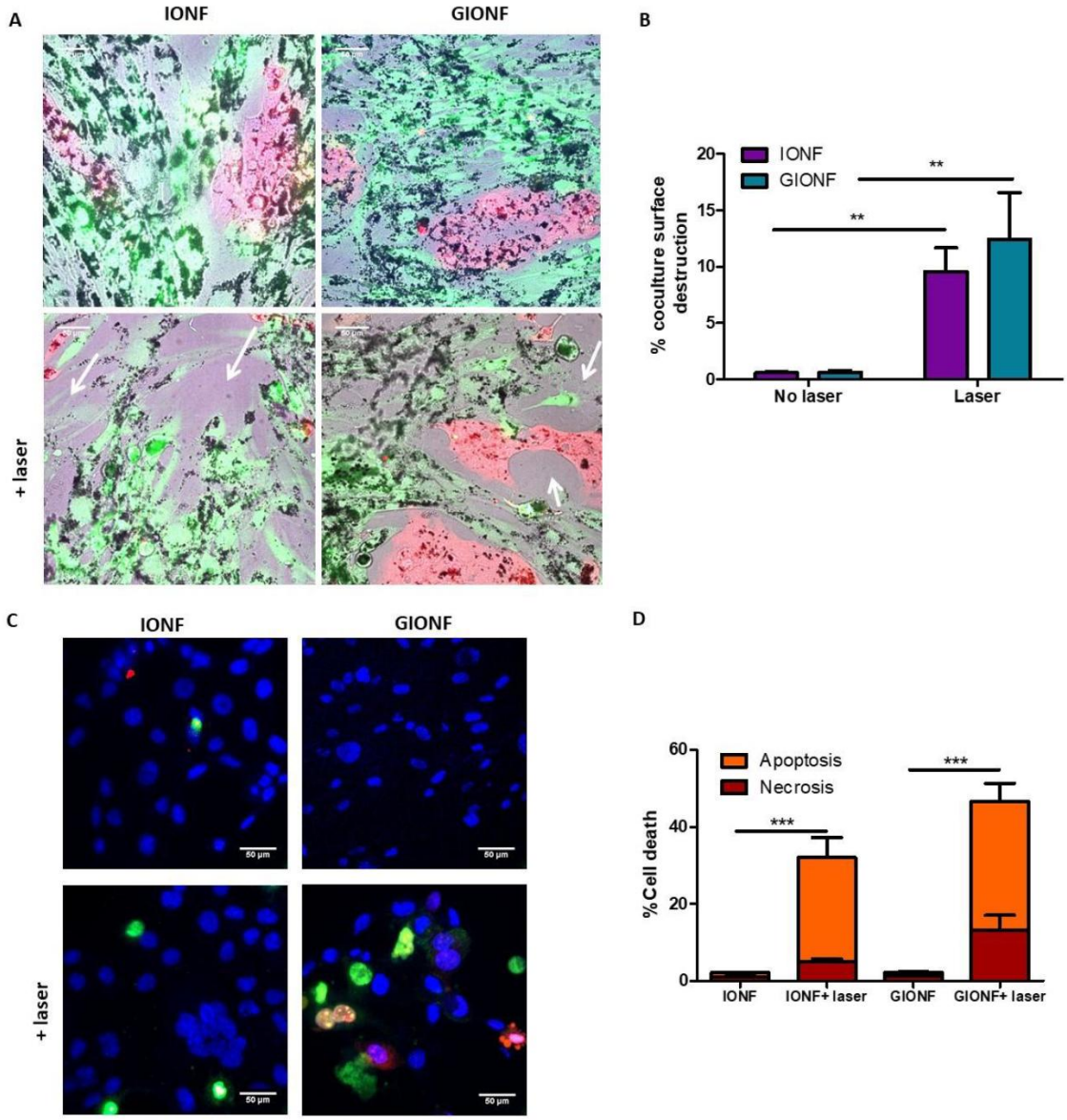

(Figure 4D).

Figure 4. GIONF and IONF-induced PTT in fibroblasts:tumor cells co-culture. A) fibroblasts (hTERT-HSC):tumor cells (EGI-1) co-culture incubated with IONF and GIONF [Fe] 112 µg/mL overnight. The cocultures were then irradiated with an 808 nm laser at 1W/cm^2 during 10 min. The destructuration of the co-culture were observed 4 hours after laser irradiations (indicated with white arrows). Scale bar = 50 µm. B) Quantification of the surface of co-culture destroyed. C) Fluorescence images of cells stained with Hoechst 33342 (cell nuclei, blue), YO-PROTM (apoptotic cells, green) and propidium iodide (necrotic cells, red). Scale bar = 50 µm D) Quantification of the cell death after GIONF and IONF-mediated PTT. Results are shown as mean ± SEM of two independent experiments. One-way ANOVA Krustal-Wallis test, Dunn's multiple comparison ***p-value<0.0001.

Distribution of GION in the Tumor Microenvironment of Human Cholangiocarcinoma Confirms CAF targeting.

Considering results obtained in solution and *in vitro* indicating higher GIONF heating efficiency, the *in vivo* experiments were only performed with GIONF. As a prototypical model of highly desmoplastic cancer, we chose a model of cholangiocarcinoma (CCA) in which the fibrotic stroma compartment takes up a large proportion of the tumor. Importantly, the human EGI-1 CCA model when implanted subcutaneously in mice accurately reproduces the architecture of human cholangiocarcinoma as shown in Figure 5A. In terms of architecture, the tumor islets and the extensive stroma compartment, occupying around 20 % of the tumor, are well separated. Fibroblasts are one of the most abundant cell types in tumor stroma and in this particular tumor, the stroma of EGI-1 tumor model is composed

mainly of αSMA+ cells and a lower proportion of F4/80+ macrophages as seen in Figure S5. Desmoplastic tumors such as CCA are also characterized for abnormally dense ECM. Tumor ECM, in particular the dense and linearized collagen network plays an important role in tumor stiffening over its progression. Considering that CAF are the main producers of stromal collagen and key actors of ECM remodeling, CAF activity, tumor stiffness evolution and tumor growth might be tightly related. For this reason, we decided to monitor simultaneously the tumor growth and the tumor stiffness evolution by means of shear wave elastography (SWE). Figure 5B-C actually demonstrates the parallel increase of tumor volume and tumor stiffness in EGI-1 model.

In this well-characterized desmoplastic tumor model, we injected 200 µg of GIONF directly in the tumor. The intratumoral injection was preferred over intravenous injection since it is clinically relevant therapeutic option for tumors that are deemed unresectable but that are accessible *via* catheter, which is often the case of the CCA. Hence we examined if GIONF intratumoral administration associated with laser irradiation (also feasible by intraluminal illumination) could be a be a therapeutic option as neoadjuvant therapy of non-resectable CCA in order to reduce the size of the tumor and eventually make it resectable. The advantage of intratumoral administration is also to maximize the amount of nanoparticles in the tumor and minimizing systemic toxicity. Current practice for the treatment of hepatocellular carcinoma comprises locoregional ablation of tumors consisting in the percutaneous injection of ethanol or the percutaneous introduction of an electrode used for the radiofrequency ablation (RFA) of the tumor under imaging guidance. Therefore, percutaneous intratumoral injection into intrahepatic CCA (10-20% of CCA) could be a feasible option. Regarding the other types of CCA (perihilar CCA (50%) and distal CCA (30-40%)), an access through an endoscopic device is currently available with the techniques of EUS-FNA (Endoscopic ultrasound-guided fine-needle aspiration) and ERCP (endoscopic retrograde cholangiography) coupled to a cholangioscopy. These devices used for

tissue aspiration or bile drainage, could be used for injection of nanoparticles. Regarding the local NIR irradiation of the tumor tissue, endoscopic devices, already developed for photodynamic therapy (PDT) and RFA in CCA, [27,28] could be adapted. For example, a stent incorporating light-emitting diodes allowed local illumination with a specific wavelength of light and activation of the photosensitizer for PDT. Here with NIR excitation (808 nm), we can expect a penetration of the NIR light about 1 cm from the endoscope extremity into the tumor tissue.

Tumor volume evolution and stiffness monitoring using SWE confirmed that GIONF injection alone did not have any effect on any of these two parameters (Figure 5B-C). Prior to performing the laser irradiation to assess the effect of PTT treatment, we decided to study the biodistribution of GIONF in EGI-1 tumor microenvironment in order to evaluate potential targets of GIONF. Since *in vitro* experiments revealed a preferential uptake of fibroblasts and to lesser extent of macrophages, we checked if this was confirmed *in vivo* in CCA xenograft mouse model. Importantly GIONF were mainly internalized by CAF identified as αSMA+ cells (Figure 5A, white arrows). This result correlated with the preferential internalization of GIONF by fibroblasts as reported above in co-culture with tumor cells as well as in monoculture. GIONF were not coupled to any kind of CAF targeting agent, hence this preferential uptake by fibroblast may seem surprising. However due to the segregation of stroma and tumor nests in EGI-1 tumors, there is a high probability that the nanoparticles encounter the stromal compartment and since the fibroblasts are the most abundant population that nanoparticles first encounter fibroblasts upon intratumoral injection of nanoparticles. Previous studies have already described an off-target distribution of nanoparticles to fibroblasts which create a barrier protecting tumor cells from cytotoxic agents.[29] This phenomenon that may at first sight, be considered as an obstacle against tumor therapy, can be exploited to target CAF instead. Notwithstanding these topological considerations, the better affinity of GIONF for fibroblasts in

comparison to the tumor cell compartment observed in *in vitro* co-culture further supports fibroblast targeting *in vivo*.

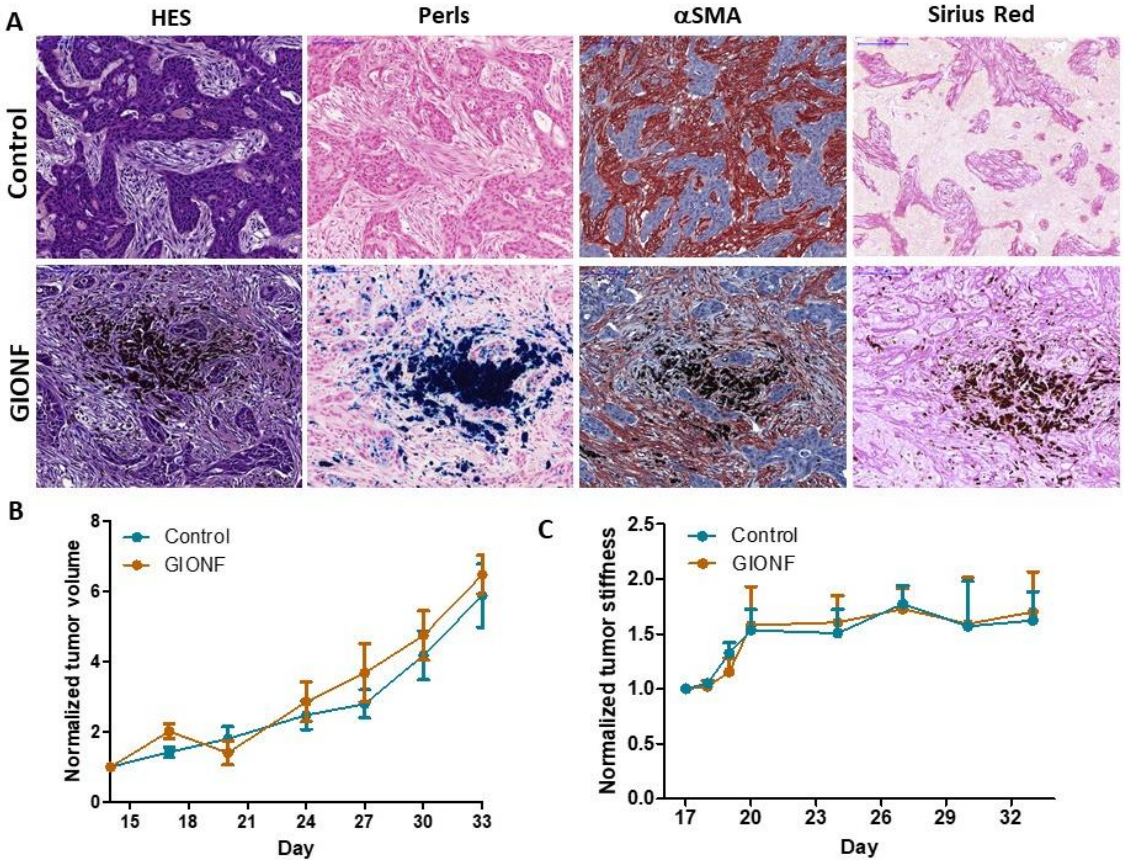

Figure 5. GIONF biodistribution in the microenvironment of EGI-1 tumor. A) Histological staining using HES, Perls (iron labelled in blue) and Sirius Red staining (collagen labelled in red/pink) and IHC (αSMA labelling, αSMA+ cells are labelled in red) analysis of GIONF injected tumors. Scale bar = 100 µm. GIONF (indicated by the white arrows) are mainly accumulated in the stroma compartment, uptaken by the αSMA+ fibroblasts. B) Normalized tumor growth evolution control (n = 10) and GIONF injected (200 µg) (n =3) EGI-1 tumors. C) Normalized mean tumor stiffness evolution of control (n=10) and GIONF (n=3) injected EGI-1 tumors. Results are represented as mean ± SEM.

GIONF-mediated PTT in Cholangiocarcinoma: the Dose Matters

Considering the preferential accumulation of GIONF in CAFs, GIONF-mediated mild hyperthermia was performed in EGI-1 tumor bearing mice with the objective of targeting CAF. In a first approach, 200 µg of GIONF were administered by intratumoral injection 30 minutes prior to laser irradiation. The tumors were exposed to 808 nm laser for 30 minutes and temperature was monitored using an infrared camera (Figure 6A). This protocol was performed three times at 24-hour interval. The average surface temperature was maintained at 43°C for 30 min (Figure 6B). The laser power was adjusted each time to maintain this average surface temperature, nevertheless the laser power remained at ≈0.9W/cm^2 meaning that the heating efficiency of intratumoral GIONF did not change significantly during the three days of treatment (Figures S6A and S6B). Tumor growth was followed up to 20 days after the last PTT session. Unfortunately, GIONF-mediated PTT did not induce tumor regression in these conditions (Figures 6D and S7A). However, we observed some changes in tumor stiffness evolution during and after the PTT treatments (Figure 6E-H).

Previous studies performed by our group showed that carbon-nanotube-mediated PTT induces changes in tumor stiffness.[30] As previously mentioned, desmoplastic tumors such as CCA are characterized by a dense and linearized collagen network plays an important role in tumor stiffening over its progression. Considering that CAF are the main producers of stromal collagen, we hypothesized that targeting CAF would induce a decrease in collagen production and consequently affect tumor stiffness. As shown in Figure 5B, the overall rigidity of EGI-1 untreated tumors increased by more than 70% from day 15 (start of SWE monitoring) to day 32 showing that SWE monitoring provides a relevant noninvasive biomarker of ECM remodeling in EGI-1 tumors. To evaluate the effect of PTT, SWE measurements were performed before each laser irradiation and at different time-points over the 20 days post-irradiation. SWE mapping of tumor stiffness showed an acute and transient stiffening

(Figures 6E and 6H) 24 hours after the first laser irradiation. This effect of increase tissue stiffness has already been seen in other heat-based therapies such a radiofrequency ablation in the heart (cardiac) and in hepatic tumors. [31,32] The alteration of the biomechanical properties of the TME towards a higher stiffness has been shown to favor tumor development. [33-35] For this reason, it is possible to hypothesize that the increased stiffness of the TME after the first PTT, may promote tumor progression in the case of inefficient PTT. However, this effect was transient and soon after the second PTT treatment the stiffness started to decrease in comparison to the untreated tumors that show gradual stiffening towards a plateau. At day 24, the percentage of stiff area (>40 kPa) was slightly lower for treated tumors although the difference was not statistically significant (Figure 6F). We also observed a significant reduction in the percentage of αSMA+ surface of tumors indicating a depletion of CAF after 3 consecutive PTT sessions in comparison to the non-treated tumors (control or GIONF only) (Figure 6 I-J). However, the tumor volume progression was the same for PTT-treated and untreated tumors in this set-up. This shows that these 3 consecutive PTT treatments at 43°C for 30 min were sufficient to start depleting the CAF population and to affect tumor stiffness transiently (transient increase followed by softening over 5 days) without changing tumor growth. However, at day 27, tumor stiffness increased again to the plateau value in parallel to tumor progression. Overall the PTT treatment reported above could not induce a sustained effect on tumor evolution.

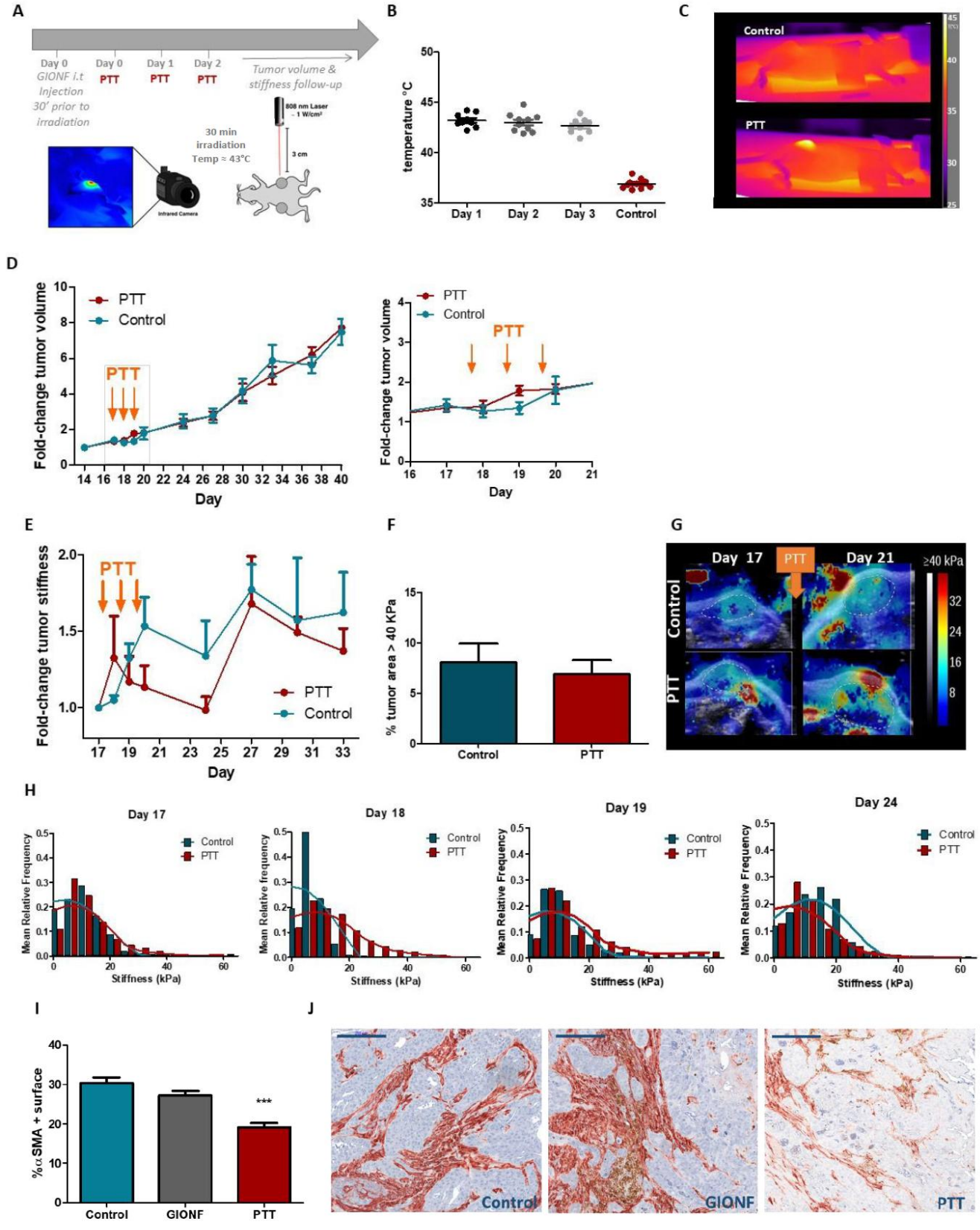
A
Day 0
GIONF i.t Injection 30' prior to irradiation
Day 0
PTT
Day 1
PTT
Day 2
PTT
Tumor volume & stiffness follow-up
808 nm Laser ~ 1 W/cm²
30 min irradiation Temp ≈ 43°C
3 cm
Infrared Camera
B
temperature °C
Day 1
Day 2
Day 3
Control
C
Control
PTT
D
Fold-change tumor volume
PTT
Control
Day
E
Fold-change tumor stiffness
PTT
Control
Day
F
% tumor area > 40 KPa
Control
PTT
G
Day 17
PTT
Day 21
≥40 kPa
Control
PTT
H
Day 17
Day 18
Day 19
Day 24
Mean Relative Frequency
Stiffness (kPa)
Control
PTT
I
%α SMA + surface
***
Control
GIONF
PTT
J
Control
GIONF
PTT

Figure 6. Low thermal dose GIONF-mediated PTT protocol in EGI-1 tumor model. A) Illustrative scheme of the low thermal dose experiment plan. B) Average surface temperature of tumors during the three PTT sessions. C) *In vivo* infrared thermal images of tumors injected with 200µg GIONF and exposed 30 minutes to an 808 nm laser. D) Normalized tumor growth evolution of control (n = 10) and PTT treated (n =10) EGI-1 tumors. Results are represented as mean ± SEM. E) Normalized mean tumor stiffness throughout the experiment of control (n=10) and PTT (n=10) treated EGI-1 tumors. Results are represented as mean ± SEM. F) Percentage of the intratumoral area exceeding the threshold of 40kPa 4 days after the last PTT session (Day 24). G) SWE color stiffness map before and after the three consecutive sessions of PTT. H) Histogram of stiffness distribution of control and PTT treated tumors at three different time points: before the first irradiation (Day 17), before the second irradiation (Day 18), before the third irradiation (Day 19) and 4 days after the last irradiation (Day 24). I) Quantification of percentage (%) of αSMA + surface of tumors at control, GIONF only and after 3 consecutive PTT sessions at low dose (1st experimental setup). Results are represented as mean ± SEM. *** *p*-value <0.001. J) Representative images of αSMA labeling in control, GIONF–injected tumors and tumors that have undergone 3 consecutive low dose PTT sessions. Scale bar = 100 µm.

The level of thermal damage of a tissue depends on tissue sensitivity, temperature and time of exposure. However, a consensus in the scientific community has been reached establishing a breakpoint in the rate of heat cell death induction at 43°C. The calculation of the cumulative equivalent minutes at 43°C (CEM43°C) is used to determine the thermal dose of a hyperthermia protocol and allows us to compare different approaches.[36] In the experiment above the CEM43°C was of 30 per session, 90 for the entire protocol. As these conditions were not enough to induce an effect on tumor growth, we designed the next approach with the aim of increasing the thermal dose. For that, the two

main parameters in the CEM43°C equation were modified: the mean temperature was increased from 43°C to 45°C, still remaining in a mild hyperthermia approach and the time of laser exposure was also significantly increased from 30 to 45 min per session. For safety reasons (non-specific heating of laser) and to keep the laser power in a permissible range (<1W/cm^2) (see Figure S6), we increased the amount of GIONF injected to ensure the temperature increase.

In this second *in vivo* GIONF-mediated approach, 700 µg of GIONF were administered by intratumoral injection 1 day prior to laser irradiation (instead of 30 min for the first experiment) in order to let some time for proper diffusion and cellular uptake of the nanoparticles within the tumor (Figure 7). The tumors were exposed to 808nm laser for 45 minutes and temperature was monitored using an infrared camera (Figure 7A). This protocol was performed three times at 24-hour interval. The average surface temperature was maintained, this time at 45°C (Figures 7B and 7C). The laser power was adjusted each time to maintain this average surface temperature, nevertheless the laser power remained at ≈0.7W/cm^2 (Figures S6C and S6D). The tumor growth was followed up to 10 days after the last PTT session. With these experimental conditions, the CEM43°C was significantly higher than that of the previous approach: 180 per session, 540 for the entire PTT protocol. An initial increase of tumor growth was observed in those animals that had undergone the first session of GIONF-mediated PTT (Figure 7D). This was followed by a steady tumor regression. A complete tumor regression was observed in 7 out of the 10 mice treated. GIONF alone and laser irradiation alone did not change tumor growth (Figure S7B). Once again, SWE was used for mapping the evolution of tumor stiffness. Tumor stiffness increased with time in control tumors, whilst it continuously decreased soon after the second PTT sessions in those that had undergone GIONF-mediated PTT (Figure 7E). Note that the rapid decrease of overall stiffness was observed at earlier time-points (from day 21) in comparison to the tumor volume which becomes lower than untreated tumor volume only at day 25.

As it can be visualized in the SWE stiffness maps, control tumors start developing very stiff regions (> 40kPa) on day 22 (Figures 7F, 7G and 7H), while treated tumors do not display such stiff regions although they have similar volumes at this time point. Hence tumor softening can be considered as an early response to the PTT treatment and stiffness mapping as a relevant physical marker to appreciate the response to the treatment.

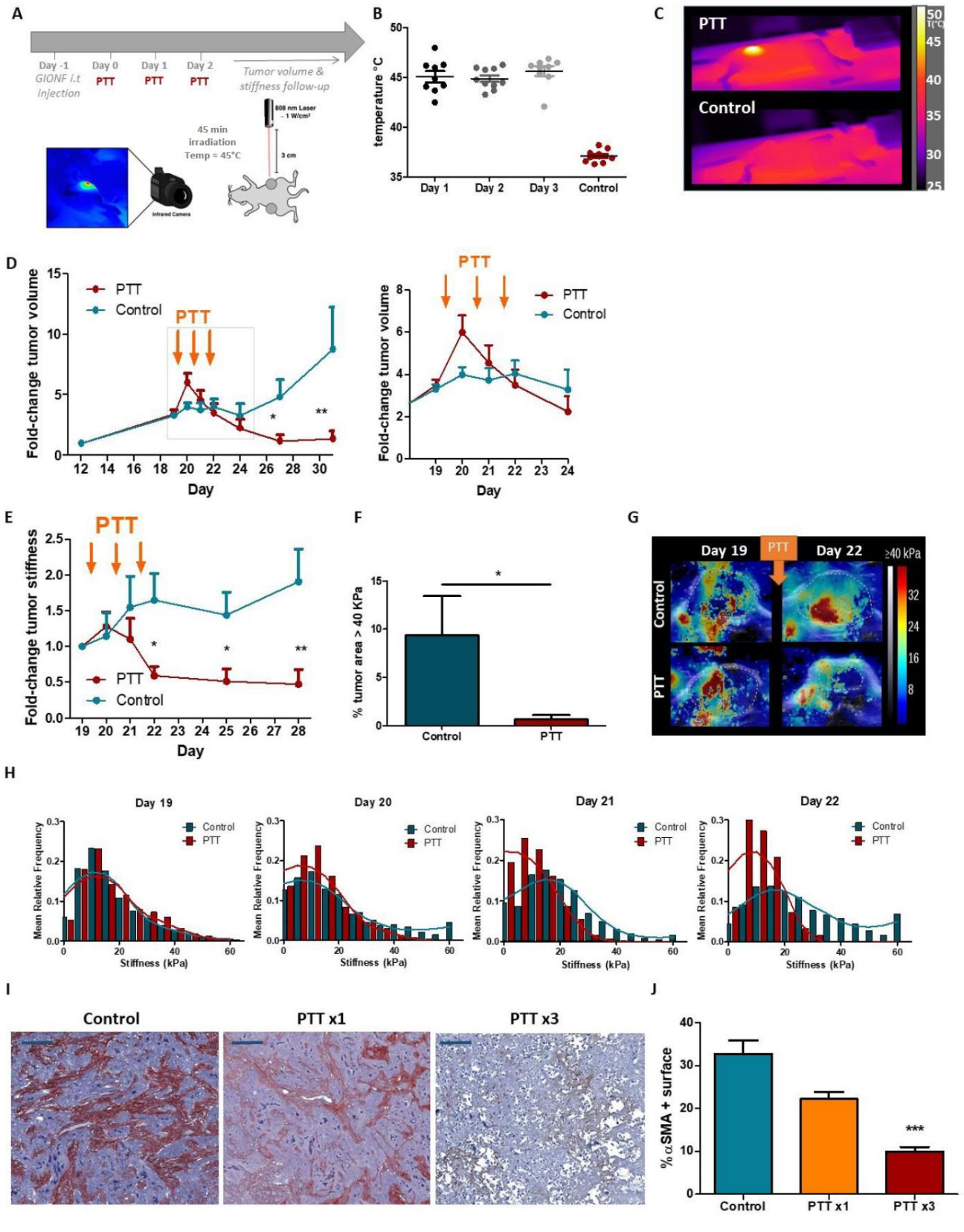
A
Day -1
GIONF i.t injection
Day 0
PTT
Day 1
PTT
Day 2
PTT
Tumor volume & stiffness follow-up
808 nm Laser
45 min irradiation
Temp ≈ 45°C
3 cm
Infrared Camera
B
temperature °C
Day 1
Day 2
Day 3
Control
C
PTT
Control
D
Fold-change tumor volume
PTT
Control
Day
E
Fold-change tumor stiffness
F
% tumor area > 40 KPa
Control
PTT
G
Day 19
PTT
Day 22
≥40 kPa
Control
PTT
H
Day 19
Day 20
Day 21
Day 22
Mean Relative Frequency
Stiffness (kPa)
I
Control
PTT x1
PTT x3
J
% αSMA + surface
Control
PTT x1
PTT x3

Figure 7. GIONF-mediated PTT reduces EGI-1 tumor growth. A) Illustrative schema of the experiment plan. B) Average surface temperature of tumors during the three PTT sessions C) *In vivo* infrared thermal images of tumors injected with 700 µg GIONF and exposed 45 minutes to an 808 nm laser D) Fold-change tumor growth evolution control (n = 10) and PTT treated (n =10) EGI-1 tumors. Results are represented as mean ± SEM. * *p*-value <0.05, ** *p*-value <0.01. E) Fold-change mean tumor stiffness throughout the experiment of control (n=10) and PTT (n=10) treated EGI-1 tumors. Results are represented as mean ± SEM. * *p*-value <0.05, ** *p*-value <0.01. F) Percentage of the intratumoral area exceeding the threshold of 40 kPa 3 days after the last PTT session (Day 24) G) SWE color stiffness map before and after the three consecutive sessions of PTT. H) Histogram of stiffness distribution of control and PTT treated tumors at three different time points: before the first irradiation (Day 19), before the second irradiation (Day 20), before the third irradiation (Day 21) and 1 day after the last irradiation (Day 22). I) Representative images of αSMA labeling in tumors that have undergone a single PTT session, the 3 consecutive PTT sessions and control tumors. Scale bare = 200 µm J) Quantification of % of αSMA + surface of tumors after a single PTT session, the 3 consecutive PTT sessions and control tumors. Results are represented as mean ± SEM. *** *p*-value <0.001.

Fibroblasts – Targeted PTT

To evaluate the overall effect produced by GIONF-mediated PTT and the rationale of 3 consecutive laser irradiations, we performed histological staining and immunohistochemistry labeling. Two mice of the control and GIONF-mediated PTT group were sacrificed after the first GIONF-mediated high thermal dose PTT session in order to evaluate the initial damages of the therapy. The images show that 40-50% of the tumor has already been damaged (necrotic) after the first session of GIONF-mediated

PTT (Figure S8A). However, Perls staining shows how most of the nanoparticles were still accumulated in the tumor stroma surrounding the tumor. In contrast, after the 3 sessions of GIONF-mediated PTT, most of the tumor was necrotic (Figure S8B). A more homogeneous distribution of the nanoparticles was observed, probably due to an increase in nanoparticle diffusion into the tumor after PTT. This confirms our previous study showing iron oxide nanocubes injected intratumorally in epidermoid carcinoma that were mostly blocked in the periphery ECM of the tumor and that successfully penetrated the core of the tumor upon excitation with an alternating magnetic field inducing mild magnetic hyperthermia (42°C).[37]

Here we also observed a recruitment of tumor-associated macrophages, identified by F4/80 labelling in the core of the necrotic area (Figure S8B, black arrows). In order to evaluate the role of CAF targeting in the mechanisms of GIONF-mediated PTT treatment, we evaluated the level of αSMA+ cells in tumors, both after the first PTT session and at the end of the treatment. The quantification of αSMA in the different tumor groups show that there is a significant decrease of αSMA+ cells in tumors that have undergone the 3 PTT sessions and to a lesser extent in those that have only gone through one high thermal dose PTT session (Figures 7I and 7J). This means that the repetition of PTT treatments increase CAF depletion. As reported above, there was also a decrease of αSMA+ cells after the three low thermal dose PTT sessions, but to a lesser extent compared to the high thermal dose (30 % of the total αSMA+ depleted at low dose (Figure 6I-J), *versus* 60% at a high thermal dose (Figure 7J)). Overall, in order to have a significant depletion of αSMA+ cells, 3 rounds of PTT at high thermal dose are needed. This result suggests the role of CAF depletion in tumor softening and regression following PTT treatment.

Other studies have also proved the effectiveness of targeting CAF by exploiting the off-target distribution of nanoparticles to fibroblasts in desmoplastic tumors. Ernesting *et al.* showed that the injection of carboxymethyl cellulose-docetaxel nanoparticles in a pancreatic adenocarcinoma murine model results in 90 % of accumulation in αSMA+ cells resulting in a long-term depletion of this cell population.[38] Another study in a bladder carcinoma model using gemcitabine and cisplatin nanoparticles administered i.v. also report a depletion of αSMA+ cells. In this study, the authors also report an eventual decrease of collagen deposition 4 days after injection.[39] In our case we have not identified any kind of modifications in the collagen tumor network. In order to test the specific effect of GIONF-mediated PTT in a collagen matrix, we used a fresh sheep tendon exposed to GION and light irradiation as a model. Results do not show any kind of destruction in the collagen matrix after 10 min irradiation at 2 W/cm^2 (Figure S9). Hence, the decrease in tumor stiffness that arises soon after PTT treatment could be related to the rapid destructuration of the tumor architecture due to hyperthermia-induced cell necrosis, including mostly fibroblasts. Fibroblast depletion could also inhibit the formation and remodeling of new ECM that is responsible for tumor stiffening in non-treated tumors and have indirect effect to inhibit tumor relapse in PTT-treated tumors.

Conclusions

The use of nanoparticle-based therapies as anti-tumor therapy has greatly been challenged by the complexity of the TME. In particular, nanoparticle-mediated PTT has been thoroughly studied in preclinical settings and is currently in clinical trials, however the fate of nanoparticles in the tumor microenvironment and the effect of this therapeutic modality on the TME is still unexplored. Other than tumor cells, there are multiple possible targets for nanoparticle-mediated PTT within the TME, one of them being CAFs. In this study we present hybrid iron oxide-gold nanoparticles, GIONFs, with optimal optical properties and degradability that make them ideal PTT agent for consecutive PTT

treatments after a single intratumoral injection of nanoparticles. Importantly the tumor temperature could be modulated during laser exposition using relatively low and safe laser power and similar tumor temperature could be obtained for three consecutive PTT treatment at 1 day interval showing the sustained heating capacity of GIONF in tumors. The fate of these nanoparticles within the TME has been deciphered, resulting in an accumulation in CAFs. This preferential accumulation in CAFs determined the therapeutic outcome and cumulative effects of PTT treatment in desmoplastic CCA

This off-target distribution of GIONF in fibroblasts can be exploited to target CAF (αSMA+ population). The efficiency of GIONF as agents for PTT in CCA could be modulated by varying the injected dose as well as the irradiation time and the number of laser expositions. At the correct thermal dose, a significant depletion of αSMA+ population is observed, particularly after three PTT treatment which shows the feasibility and rationale of repeated treatments. This is accompanied by an early and significant reduction of tumor stiffness followed by tumor regression. Tumor regression was not only induced by the depletion of αSMA+ cells, but also the mechanical changes in the tumor microenvironment may have favored the phenotypic modification of tumor cells.[40]

Our results demonstrate that CAF-targeted PTT modulates the physical properties of the solid tumors, in this case CCA, modulating tumor stiffness, subsequently followed by tumor regression. We demonstrate, for the first time, the potential of repeated CAF-targeted PTT for the treatment of desmoplastic tumors after intratumoral administration. GIONF-mediated PTT could be a valuable clinical option to soften and shrink unresectable fibrotic tumors after a single injection of nanoparticles and repeated laser exposure, with eventual synergetic combination with standard of care chemo or radiotherapy.

Methods/Experimental

IONF synthesis

IONF were synthesized following the procedure published by Hugounenq *et al.* [16] $FeCl_3.6H_2O$ (2.164 g; 8 mmol) and $FeCl_2.4H_2O$ (0.398 g; 2 mmol) were completely dissolved in DEG (75 mL). The solution was stirred for one hour. The black-colored solution was poured with NMDEA (75 mL) and stirred again for one hour. Separately, NaOH pellets (1.42 g; 35.6 mmol) were dissolved in a mixture of polyols (40 mL DEG and 40 mL NMDEA). This solution was added to the solution of iron chlorides and the resulting mixture was stirred for another three hours. Then, the temperature was elevated to 220°C using a regular heating ($2°C.min^{-1}$)). Once the temperature is set to 220°C, the solution is stirred for 4 hours, and then cooled down slowly to room temperature by removing the heating plate. The black sediment was separated magnetically and washed with mixture of ethanol and ethyl acetate (1:1, v/v) for several times to eliminate organic and inorganic impurities. Possible iron hydroxides were removed by treatment with 10% nitric acid. Iron(III) nitrate ($Fe(NO_3)_3.9H_2O$) (2 g, $4.951x10^{-3}$ mol) is then dissolved in water (20 mL) and added to the nanoparticles. The resulting mixture is heated to 80°C for 45min to achieve a complete oxidation of the nanoparticles. After another treatment with 10% nitric acid, the particles were washed twice with acetone and diethyl ether and redispersed in water. At this stage, an aqueous dispersion of maghemite nanoparticles is stable in acid or basic conditions with a point of zero charge near pH 7.3.

Synthesis of gold decorated IONP (GIONF)

Chelator-coated gold nanoparticles functionalized with dopamine (Au@DTDTPAd) - An aqueous solution (3 mL) containing EDC (0.207g; $1{,}08 \times 10^{-3}$ mol) and NHS (0.247g; $2{,}150 \times 10^{-3}$ mol) was added to a suspension of Au@DTDTPA gold nanoparticles (6 mL, 10g Au/L). The synthesis and the complete characterization of Au@DTDTPA were described elsewhere.[23] These gold nanoparticles are composed of a gold core (2-3 nm) which are coated with dithiolated derivative of diethylenetriaminepentaacetic acid (DTDTPA). The suspension was stirred at pH 6 for 90 minutes. Afterwards, an aqueous solution (4 mL) containing dopamine (9.45×10^{-3}g; 2.25×10^{-5} mol) was added to the suspension under stirring at pH 7.5. The mixture is stirred overnight. The purification of the suspension of gold nanoparticles was performed by dialysis against water (MWCO: 6-8 kDa) for 12 h. Water bath was changed three times every 3 h.

Assembly of Au@DTDTPAd with IONF - Under stirring, the suspension of Au@DTDTPA modified by dopamine (Au@DTDTPAd) was mixed with the suspensions of maghemite nanoflowers (IONFs, 6 mL; 35 g Fe/L). The mixture with a pH of 5.5 was heated at 50°C for 24 h. Successive washings were performed with ultrapure water, acetone, and diethyl ether until a clear supernatant was obtained. After purification the iron oxide nanoflowers decorated with gold nanoparticles (GIONFs) were introduced in ultrapure water (6 mL) in order to provide an aqueous suspension of GIONFs with an iron concentration of 35 $g.L^{-1}$.

The size and the morphology of IONF and GIONFs, *i.e.* maghemite nanoflowers before and after the assembly with the gold nanoparticles, were observed by transmission electron microscopy (JEOL JEM 2100F microscope at 200 kV (ICB, Dijon, France)). Drops of colloidal solutions were deposited on dedicated TEM carbon grids and observed after natural drying at room temperature.

Nanoparticles photothermal measurements

100 µL of IONF and GIONF solutions were prepared at [Fe]=1mg/mL and 100µg/mL in water in a 500 µL microtube. The solution was exposed to an 808 nm beam laser for 5 min (2.2 W/cm^2, height 4 cm from the liquid/air interface, Laser Diode Drivers, BWT), and temperature was recorded with an infrared camera SC7000 from FLIR Systems. Optical specific absorption rate (SAR) was calculated as published before.[41] The initial temperature slope, *i.e.* the first 30 s, dT/dt slope after laser switch-on, was measured, and SAR was calculated according to: SAR=CV/m dT/dt, where m is the total mass of Fe in the sample, C is the specific heat capacity of the sample (C_{water} = 4185 J/L/K), and V is the sample volume.

Cell culture

EGI-1, tumor cells derived from extrahepatic CCA, obtained from the German Collection of Microorganisms and Cell Cultures (DSMZ, Germany), were cultured in DMEM supplemented with 1 g/L glucose, 10 mmol/L HEPES, 10% fetal bovine serum (FBS), antibiotics (100 UI/mL penicillin and 100 µg/mL streptomycin) and antimycotic (0.25 µg/mL amphotericin B) (Invitrogen). Murine macrophage-like cell line RAW264.7 (ATCC, TIB-71), hTERT-HSC derived from human activated immortalized hepatic stellate cells kindly provided by Dr. L. Aoudjehane (ICAN, Paris, France) and HUVEC (ATCC CRL-1730) were cultured in DMEM supplemented with 10 % Fetal bovine serum (FBS), Penicillin/Streptomycin, L-Glucose and Sodium pyruvate (Gibco).

Lentiviral infection for the generation of mCherrry and GFP cells

In order to obtain a stable expression of mCherry and GFP in EGI-1 and hTERT-HSC cells, respectively, we used a transduction technique with lentivirus. Plasmid containing the coding sequence for mCherry designed by GenecopoeiaTM (Maryland, USA) were used to generate □U3 SIN lentivirus in the Viral and Gene Transfer Vectors Platform of Necker (Paris, France) according to the

regulations. GFP coding lentivirus was commercially available. Positive transduced cells were detected by positive fluorescence signal and they were selected by treatment with lethal doses of puromycin for 72h to eliminate non-infected cells.

In vitro cellular uptake of GIONF/IONF and cellular photothermal measurements

EGI-1 cells were incubated with [Fe] 112µg/ml GIONF or IONF for 24 h in 6-well cell culture plates. Cells were then trypsinized, washed with PBS1X and counted. 1x 10^6 cells were resuspended in 100µl PBS 1X (500 µl tube). The cell suspension was then subjected to an 808 nm beam laser for 5 min (2.2 W/cm^2, height 4 cm from the liquid/air interface, Laser Diode Drivers, BWT), and temperature was recorded with infrared camera SC7000 from FLIR Systems.

Quantification of GIONF uptake by cells *in vitro*

In order to study the uptake of GIONF and IONF in cells when incubated at different concentrations ([Fe] 112, 56 and 11.2 µg/mL) for 24 hours, the concentration of iron in EGI-1 cells, hTERT and RAW264.7 cells was performed by ICP atomic emission spectrometer (model iCAP6200 duo. Thermo Fischer Scientific, analysis performed in the PARI platform, IPGP, Paris, France). For each iron measurement, cell pellets were digested in 289 µL of 69% nitric acid (trace metal basic grade; Sigma) at room temperature overnight. The solutions were then diluted in ultrapure water for analysis. The calibration standards and the quality controls were provided by SCP SCIENCE and ChemLab. The analyzer drift is regularly corrected by quality controls measurements to ensure a drift lower than 5%.

An ASX-520 Autosampler was used. Argon 4.5 Linde (min, 99.995%) was used as plasma and purge gas. All samples were analyzed in 2% nitric acid.

The concentration of gold in EGI-1 was also performed by ICP atomic emission spectrometer. For each gold measurement, cell pellets were digested in 1.5 mL of aqua regia (1mL hydrochloric acid 37% and 500µL nitric acid 69%) in a boiling oil bath, until all liquid was evaporated. The pellet was then solubilized in a 1% HCl solution for the Au analysis. Calibration standards and quality controls were provided by SCPSCIENCE and ChemLab.

Transmission Electron Microscopy (TEM)

TEM images were acquired using a Hitachi HT7700 operating at 80 kV (MIMA2 platform, INRA, Jouy-en- Josas, France). EGI-1 cells were incubated with GIONF or IONF at iron concentration of [Fe] 112 µg/mL for 24 hours at 37°C. Following incubation cells (EGI-1 and MET-1) were detached by trypsinization, washed twice with PBS and fixed with 2% glutaraldehyde in 0.1 M Na cacodylate buffer pH 7.2, for 1 hour at room temperature. Samples were then contrasted with Oolong Tea Extract (OTE) 0.5% in cacodylate buffer for 1 hour at room temperature, postfixed with 1% osmium tetroxide containing 1.5% potassium cyanoferrate for 1 hour at room temperature, gradually dehydrated in ethanol: 70% 5min incubation, 90% - 5 min incubation, 100% - 5min incubation 3 times. Ethanol was then substituted gradually in mix of ethanol-Epon under vacuum for 1 hour and finally embedded in Epon. (Delta microscopie – Labège France). Thin sections (70 nm) were collected onto 200 mesh copper grids, and counterstained with lead citrate. Grids were examined with Hitachi HT7700 electron microscope operated at 80kV (Elexience – France), and images were acquired with a charge-coupled device camera (AMT).

IONF/GIONF cytotoxicity

Nanoparticle cytotoxicity was evaluated using Alamar Blue assay (Life Technologies). Cell viability was checked after incubation with different nanoparticle concentration ([Fe] 10, 50, 100, 200 and 500 μg/mL) for 24 hours. EGI-1, hTERT, HUVEC and RAW 264.7 cells were incubated with GIONF and IONF at different concentrations in DMEM supplemented with 10% FBS and 1% Penicillin/Streptomycin at 37 °C in 48 well plates (≈ 9 x10^4 cells) for 24 hours. The medium was then removed and the cells were washed with cell culture medium. Cells were then incubated with 10% Alamar Blue in DMEM without phenol red for 2 hours. The medium was then transferred to a 96-well plate for analysis with a microplate reader (EnSpire Multimode Plate Reader, Pelkin Elmers, Waltham, MA, USA) at an activation wavelength of 550nm, with fluorescence detection at 590 nm. Cell viability was determined by comparing with control cells (no nanoparticle exposure). Cells incubated with DMSO 10% were used as a positive control (high cytotoxicity). All experiments were performed in triplicate.

IONF/GIONF hemolysis

Red blood cells were recovered and isolated from an anonymous human donor. 20 x solutions of the desired final concentration of GIONF and IONF were prepared. To perform the hemolysis assay 10 μL of the teste solutions were mixed with 190 μL red blood cells. The final test concentration of GIONF and IONF were 1000, 500, 100 and 50 μg/mL. As a positive control 1% of Triton X-100 was used. The solutions were incubated at 37°C for 30 minutes. The samples were then centrifuged at 2500 x g for 5 minutes. The supernatant was then collected and transferred to a 96-well plate for analysis with a microplate reader (EnSpire Multimode Plate Reader, Pelkin Elmers, Waltham, MA, USA) and absorbance was read at 541 nm.

2D co-culture model, nanoparticle distribution in the co-culture and cell death assays

$2x10^5$ EGI-1-mCherry and $2x10^5$ hTERT-GFP were seeded in 1 well lab-teks chambers in DMEM supplemented with 10 % FBS, Penicillin/Streptomycin, L-Glucose and Sodium pyruvate (Gibco) for 5-7 days. Fresh medium was replaced every 2-3 days. At confluence, co-culture was incubated with [Fe] 112µg/mL GIONF or IONF for 24 hours. Non-internalized particles were washed away with PBS. The cells were viewed using an Andor Technology with Olympus JX81/BX61 Device/Yokogawa CSU Device spinning disk microscope (Andor Technology plc, Belfast, Northern Ireland) using appropriate filters. Images were then analyzed using ImageJ software.

To test the whether GIONF and IONF mediated PTT in 2D co-culture induced damage to the cells, the co-cultures that had previously been exposed 24 hours to GIONF or IONF ([Fe] 112µg/mL), were irradiated with an 808 nm beam laser for 10 min (2 W/cm^2, height 4 cm from the slice, Laser Diode Drivers, BWT). Cell necrosis and apoptosis were evaluated, 4 hours after irradiation. To do so, Chromatin Condensation & Membrane Permeability Dead Cell Apoptosis Kit, purchased from Molecular Probes-Invitrogen Detection Technologies (Eugene, OR), was used according to the manufacturer's protocol. Briefly, the cells were washed with PBS and incubated with 1 µl each of Hoechst 33342 stock solution, YO-PRO^{TM} and propidium iodide stock solution at 37°C in an atmosphere of 5% CO_2 for 15 min. The cells were viewed using an Andor Technology with Olympus JX81/BX61 Device/Yokogawa CSU Device spinning disk microscope (Andor Technology plc, Belfast, Northern Ireland) using appropriate filters. The dead cells were stained with red-fluorescent propidium iodide dye whilst the apoptotic cells were stained with YO-PRO^{TM}. Blue-fluorescent Hoechst 33342 stains the chromatin of the cells, allowing to identify all the cell nuclei. Thirty images were taken for each condition. All experiments were performed three times. To quantify the level of

cell death, the number of propidium iodide labeled nuclei as well as Hoechst 33342 labeled nuclei were counted using ImageJ Cell Counter plugin.

PTT on sheep tendon and second harmonic generation imaging

Fresh sheep tendon was obtained from our local butcher. Tendon was cut (perpendicular to the fibers' orientation) using a sharp scalpel into 1-2 cm-sized fragments, which were embedded in 5% low-gelling-temperature agarose (type VII-A; Sigma-Aldrich) prepared in PBS. Slices (100 μm) were cut (parallel to the fibers' direction) with a vibratome (VT 1000S; Leica) in a bath of ice-cold PBS. The slices were then placed on top of 0.4-μm organotypic culture inserts (Millicell, Millipore) in 35-mm petri dishes containing 1.1 mL RPMI 1640 without Phenol Red. [Fe] 100 μg of GIONF were deposited on the slices. The slices were then incubated for 2 hours at 37°C to allow GIONF penetration into the tissue. The slices were washed to remove all GIONF that had not penetrated the slice. The slices were then irradiated with an 808 nm beam laser for 10 min (2 W/cm^2, height 4 cm from the slice, Laser Diode Drivers, BWT). In order to evaluate the damage produced by the GIONF-mediated PTT on the collagen network, the slices were imaged using inverted stand Leica SP5 microscope (Leica Microsystems GmbH, Wetzlar, Germany) coupled to a femtosecond Ti:sapphire laser (Chameleon, Coherent, Saclay, France) tuned at a wavelength of 810 or 850 nm for all experiments. The laser beam was circularly polarized and a Leica Microsystems HCX IRAPO 25×/0.95 W objective was used. Second harmonic generation (SHG - collagen structure) signal was detected in epi-collection through a 405/15nm bandpass filter and detected by NDD PMT detectors (Leica Microsystems) with a constant voltage supply, at constant laser excitation power, allowing direct comparison of SHG intensity values.

Tumor model and *in vivo* PTT experiments

Animal experiments were performed in accordance with the French Animal Research Committee guidelines and all procedures were approved by a local ethic committee (No 14678). $2x10^6$ cells suspended in 60 µL of PBS were mixed with 60 µL of Matrigel® growth factor reduced (Corning) and implanted subcutaneously into the flank of 5-week-old female NMRI-nu (nu/nu) mice (Envigo, France). Mice were housed under standard conditions in individually ventilated cages enriched with a nesting material and kept at 22°C on a 12-h light/12-h dark cycle with *ad libitum* access to food and tap water. Tumor growth was followed with a caliper, and tumor volume (V) was calculated as follows: xenograft volume = $xy^2/2$ where x is the longest and y, the shortest of two perpendicular diameters. When the tumor volume reached 150-200 mm^3 (approximately 18-20 days after the injection of EGI-1 cells), tumors were considered ready for treatment.

Prior to treatment animals were randomized into four groups as follows: (i) Control group: PBS intratumoral (i.t.) injection (ii) Laser control group: PBS i.t injection combined with three 808 nm laser irradiation at ~0.8 W/cm^2 for 15 min or 45 min (height from tumor skin 4 cm, Laser Diode Drivers, BWT) at one day interval, (iii) GIONF control group: 200µg or 700µg/tumor GIONF injected i.t. (iv) [Fe] 200µg or 700µg/tumor GIONF i.t injection combined with three PTT sessions (808-nm laser irradiation at ~0.8 W/cm^2 for 15 min or 45 min (height from tumor skin 4 cm, Laser Diode Drivers, BWT) at one day interval. Surface temperature was recorded with an infrared camera SC7000 from FLIR Systems during the laser treatment and analyzed using ResearchIR Software (FLIR). Two mice of each group were sacrificed after the first PTT session and after the third in order to evaluate the damages of GIONF-mediated PTT at different time-points. These mice were not included in the tumor growth and tumor stiffness analysis. All animal experiments were performed in agreement with institutional animal use and care regulations after approval by the local Ethics Committee. The

cumulative number of equivalent minutes at 43°C (CEM43°C) was calculated in each of the experiments:

$$CEM43°C = \sum_{i=1}^{n} t_i \cdot R^{(43-T)}$$

where ti is the i-th time interval, R is related to the temperature dependence of the rate of cell death (R(T< 43 °C)=1/4, R(T>43 °C)=1/2) and T is the average temperature during time interval ti. [36]

Shear wave elastography

Shear wave elastography (SWE) measurements were performed before each laser irradiation and every 3-4 days during the entire follow-up of the tumor growth. Images were acquired with the ultrasound device Aixplorer (SuperSonic Imagine, Aix-en-Provence, France) using a 15-MHz superficial probe dedicated to research (256 elements, 0.125 µm pitch). The mice were anesthetized with 2% isoflurane and their body temperature was maintained at physiological level using a heating plate. B-mode images and SWE images were acquired simultaneously. The B-mode image allowed us manually determine the region of interest (ROI) corresponding to the tumor contours. SWE mode was performed using the penetration mode with a color scale ranging from 0 (transparent) to 40 kPa (red), arbitrarily chosen in the beginning of the study according to the expected stiffness values. The area, the diameter and a set of stiffness values (mean, minimum, maximum and standard deviation) were recorded for the ROI as previously defined. SWE images were also analyzed using an in-house MATLAB code to recover the stiffness map.

Histology and immunohistochemistry

For most of the tumors, half was fixed overnight at 4 °C in a periodate–lysine–paraformaldehyde solution [0.05 M phosphate buffer containing 0.1 M L-lysine (pH 7.4), 2 mg/mL NaIO4, and 10 mg/mL paraformaldehyde]. The tumors were dehydrated in graded solutions of ethanol and embedded in paraffin. For histology, five micrometer tissue sections were stained with hematoxylin / eosin / Saffron (HES), Sirius Red staining and Perls staining.

For immunohistochemistry labelling, five micrometer tissue sections were dewaxed. For F4/80 labeling, the antigen was retrieved with citrate solution (pH 7) preheated for 10 min at 95-98°C. Endogenous peroxide was blocked for 10 min with 10% of hydrogen peroxide. The F4/80 antibody (D2S9R clone, Cell Signaling) was incubated at a 1/100 dilution. An automated staining system (Leica Bond) was used to perform the immunostaining. The anti-F4/80 antibody was detected with a secondary anti-rabbit antibody, coupled to a HRP-coupled polymer (Leica, Bond Polymer Refine Detection, No. DS9800). For αSMA labelling, sections were incubated with hydrogen peroxide for 5 min, with Protein Block (Novolink Polymer Detection System, Novocastra Laboratories, Ltd.) for 5 min and with the anti-αSMA (1A4 clones, Dako) antibody 30 min at a 1/300 dilution. Novolink Post Primary was then applied for 15 min. The sections were then washed and incubated with Novolink Polymer 15 min. An automated staining system (Autostainer Plus, Dakcoytomation) was used for immunostaining. Finally, the color was developed using amino-ethyl-carbazole (AEC substrate kit, Vector Laboratories). Sections were counterstained with haematoxylin.

Statistical analysis

Results were analyzed using GraphPad Prism 5.0 statistical software. Data are shown as mean ± standard error of the mean (SEM). For comparisons between two groups, parametric Student t-test or non-parametric Mann-Whitney test were used. For comparisons between more than two groups,

parametric One-Way analysis of variance (ANOVA) test followed by a posteriori Kruskal-Walis test and Dunn's multiple comparison test.

Supporting Information available. Supplementary Figures S1 to S9 This material is available free of charge *via* the Internet at http://pubs.acs.org.

Figure S1. UV-vis-NIR absorption spectra of GIONF and IONF at different concentrations.

Figure S2. IONF and GIONF are not cytotoxic to EGI-1, hTERT, RAW 264.7 and HUVEC cells.

Figure S3. GIONF and IONF do not induce hemolysis in red blood cells.

Figure S4. Quantification of gold in EGI-1 cells by ICP-AES.

Figure S5. Analysis of the components of the stromal compartment in EGI-1 tumor using IHC.

Figure S6. Laser power used in the *in vivo* experiments.

Figure S7. Normalized tumor volume of GIONF mediated PTT

Figure S8. Histological (HES, Perls and Sirius Red staining) and IHC (F4/80 and αSMA labelling) analysis of GIONF injected tumors after one PTT session, after the 3 PTT sessions

Figure S9. GIONF-mediated PTT does not induce collagen denaturation.

ACKNOWLEDGMENTS

We acknowledge Tatiana Ledent from Housing and experimental animal facility (HEAF), and Fatiha Merabtene and Brigitte Sohlonne from the histomorphology platform, Centre de Recherche Saint-Antoine (CRSA), Christine Péchoux (INRA, UMR 1313, Plateforme MIMA2, Jouy en Josas, France) for electron microscopy preparation and observation, Maryline Favier, Fabiola Ely-Marius and Rachel Onifarasoaniania from HistIM Plate-Form (Institut Cochin, Paris France), Laure Cordier for ICP-AES measurements that were supported by IPGP

multidisciplinary program PARI, and by Paris–IdF region SESAME Grant no. 12015908 and Dr Sylvie Fabrega from the « Viral Vector and Gene Transfer Platform, Université Paris Descartes Sorbonne Paris Cité, SFR Necker, US 24, 75014 Paris, France » for lentiviral production. We also thank Dr. Marine Camus, endoscopist from the Hôpital Saint-Antoine, for helpful discussions.

This project was funded by ANR CARGOLD (ANR-16-CE09-0026), European Union's Horizon 2020 research and innovation program under grant agreement N°685795 (NoCanTher) and the European Union's Horizon 2020 research and innovation program under grant agreement N°801305 (NanoTbTech). ANB received a PhD fellowship by the Institute thematique multi-organismes (ITMO) Cancer and the doctoral school Frontières du Vivant (FdV) – Programme Bettencourt. LF and JV are member of the European Network for the Study of Cholangiocarcinoma (ENSCCA) and participates in the initiative COST action EURO-CHOLANGIO-NET granted by the COST Association (CA18122).

References

1. Banales, J. M.; Cardinale, V.; Carpino, G.; Marzioni, M.; Andersen, J. B.; Invernizzi, P.; Lind, G. E.; Folseraas, T.; Forbes, S. J.; Fouassier, L.; Geier, A.; Calvisi, D. F.; Mertens, J. C.; Trauner, M.; Benedetti, A.; Maroni, L.; Vaquero, J.; Macias, R. I.; Raggi, C.; Perugorria, M. J. *et al.* Expert Consensus Document: Cholangiocarcinoma: Current Knowledge and Future Perspectives Consensus Statement from the European Network for the Study of Cholangiocarcinoma (ENS-CCA). *Nature reviews. Gastroenterology & hepatology* **2016,** *13*, 261-280.

2. Valle, J.; Wasan, H.; Palmer, D. H.; Cunningham, D.; Anthoney, A.; Maraveyas, A.; Madhusudan, S.; Iveson, T.; Hughes, S.; Pereira, S. P.; Roughton, M.; Bridgewater, J., Cisplatin

plus Gemcitabine *versus* Gemcitabine for Biliary Tract Cancer. *The New England journal of medicine* **2010,** *362*, 1273-1281.

3. Fabris, L.; Perugorria, M. J.; Mertens, J.; Bjorkstrom, N. K.; Cramer, T.; Lleo, A.; Solinas, A.; Sanger, H.; Lukacs-Kornek, V.; Moncsek, A.; Siebenhuner, A.; Strazzabosco, M., The Tumour Microenvironment and Immune Milieu of Cholangiocarcinoma. *Liver international : official journal of the International Association for the Study of the Liver* **2019,** *39*, 63-78.

4. Sulpice, L.; Rayar, M.; Desille, M.; Turlin, B.; Fautrel, A.; Boucher, E.; Llamas-Gutierrez, F.; Meunier, B.; Boudjema, K.; Clement, B.; Coulouarn, C., Molecular Profiling of Stroma Identifies Osteopontin as an Independent Predictor of Poor Prognosis in Intrahepatic Cholangiocarcinoma. *Hepatology* **2013,** *58*, 1992-2000.

5. Curnis, F.; Sacchi, A.; Corti, A., Improving Chemotherapeutic Drug Penetration in Tumors by Vascular Targeting and Barrier Alteration. *J Clin Invest* **2002,** *110* (4), 475-482.

6. Jain, R. K.; Stylianopoulos, T., Delivering Nanomedicine to Solid Tumors. *Nature reviews. Clinical oncology* **2010,** *7*, 653-664.

7. Eikenes, L.; Bruland, O. S.; Brekken, C.; Davies Cde, L., Collagenase Increases the Transcapillary Pressure Gradient and Improves the Uptake and Distribution of Monoclonal Antibodies in Human Osteosarcoma Xenografts. *Cancer research* **2004,** *64*, 4768-4773.

8. Kalluri, R., The Biology and Function of Fibroblasts in Cancer. *Nature reviews. Cancer* **2016,** *16*, 582-598.

9. Hayashi, M.; Yamamoto, Y.; Ibusuki, M.; Fujiwara, S.; Yamamoto, S.; Tomita, S.; Nakano, M.; Murakami, K.; Iyama, K.; Iwase, H., Evaluation of Tumor Stiffness by Elastography is Predictive for Pathologic Complete Response to Neoadjuvant Chemotherapy in Patients with Breast Cancer. *Annals of surgical oncology* **2012,** *19*, 3042-3049.

10. Mertens, J. C.; Fingas, C. D.; Christensen, J. D.; Smoot, R. L.; Bronk, S. F.; Werneburg, N. W.; Gustafson, M. P.; Dietz, A. B.; Roberts, L. R.; Sirica, A. E.; Gores, G. J., Therapeutic Effects of Deleting Cancer-Associated Fibroblasts in Cholangiocarcinoma. *Cancer research* **2013,** *73*, 897-907.

11. Riley, R. S.; Day, E. S., Gold Nanoparticle-mediated Photothermal Therapy: Applications and Opportunities for Multimodal Cancer Treatment. *Wiley interdisciplinary reviews. Nanomedicine and nanobiotechnology* **2017,** *9*.

12. Nie, L.; Wang, S.; Wang, X.; Rong, P.; Ma, Y.; Liu, G.; Huang, P.; Lu, G.; Chen, X., *In Vivo* Volumetric Photoacoustic Molecular Angiography and Therapeutic Monitoring with Targeted Plasmonic Nanostars. *Small (Weinheim an der Bergstrasse, Germany)* **2014,** *10*, 1585-93, 1441.

13. Das, R.; Rinaldi-Montes, N.; Alonso, J.; Amghouz, Z.; Garaio, E.; Garcia, J. A.; Gorria, P.; Blanco, J. A.; Phan, M. H.; Srikanth, H., Boosted Hyperthermia Therapy by Combined AC Magnetic and Photothermal Exposures in Ag/Fe3O4 Nanoflowers. *ACS applied materials & interfaces* **2016,** *8*, 25162-25169.

14. Jaque, D.; Martinez Maestro, L.; del Rosal, B.; Haro-Gonzalez, P.; Benayas, A.; Plaza, J. L.; Martin Rodriguez, E.; Garcia Sole, J., Nanoparticles for Photothermal Therapies. *Nanoscale* **2014,** *6*, 9494-9530.

15. Curcio, A.; Silva, A. K. A.; Cabana, S.; Espinosa, A.; Baptiste, B.; Menguy, N.; Wilhelm, C.; Abou-Hassan, A., Iron Oxide Nanoflowers @ CuS Hybrids for Cancer Tri-Therapy: Interplay of Photothermal Therapy, Magnetic Hyperthermia and Photodynamic Therapy. *Theranostics* **2019,** *9*, 1288-1302.

16. Hugounenq, P.; Levy, M.; Alloyeau, D.; Lartigue, L.; Dubois, E.; Cabuil, V.; Ricolleau, C.; Roux, S.; Wilhelm, C.; Gazeau, F.; Bazzi, R., Iron Oxide Monocrystalline Nanoflowers for Highly Efficient Magnetic Hyperthermia. *The Journal of Physical Chemistry C* **2012,** *116*, 15702-15712.

17. Lartigue, L.; Hugounenq, P.; Alloyeau, D.; Clarke, S. P.; Levy, M.; Bacri, J. C.; Bazzi, R.; Brougham, D. F.; Wilhelm, C.; Gazeau, F., Cooperative Organization in Iron Oxide Multi-Core Nanoparticles Potentiates their Efficiency as Heating Mediators and MRI Contrast Agents. *ACS Nano* **2012,** *6*, 10935-10949.

18. Javed, Y.; Lartigue, L.; Hugounenq, P.; Vuong, Q. L.; Gossuin, Y.; Bazzi, R.; Wilhelm, C.; Ricolleau, C.; Gazeau, F.; Alloyeau, D., Biodegradation Mechanisms of Iron Oxide Monocrystalline Nanoflowers and Tunable Shield Effect of Gold Coating. *Small (Weinheim an der Bergstrasse, Germany)* **2014,** *10*, 3325-3337.

19. Volatron, J.; Carn, F.; Kolosnjaj-Tabi, J.; Javed, Y.; Vuong, Q. L.; Gossuin, Y.; Menager, C.; Luciani, N.; Charron, G.; Hemadi, M.; Alloyeau, D.; Gazeau, F., Ferritin Protein Regulates the Degradation of Iron Oxide Nanoparticles. *Small (Weinheim an der Bergstrasse, Germany)* **2017,** *13*.

20. Miladi, I.; Alric, C.; Dufort, S.; Mowat, P.; Dutour, A.; Mandon, C.; Laurent, G.; Brauer-Krisch, E.; Herath, N.; Coll, J. L.; Dutreix, M.; Lux, F.; Bazzi, R.; Billotey, C.; Janier, M.; Perriat, P.; Le Duc, G.; Roux, S.; Tillement, O., The *In Vivo* Radiosensitizing Effect of Gold Nanoparticles Based MRI Contrast Agents. *Small (Weinheim an der Bergstrasse, Germany)* **2014,** *10*, 1116-1124.

21. Balfourier, A.; Luciani, N.; Wang, G.; Lelong, G.; Ersen, O.; Khelfa, A.; Alloyeau, D.; Gazeau, F.; Carn, F., Unexpected Intracellular Biodegradation and Recrystallization of Gold

Nanoparticles. *Proceedings of the National Academy of Sciences of the United States of America* **2020,** *117*, 103-113.

22. Walkey, C. D.; Olsen, J. B.; Guo, H.; Emili, A.; Chan, W. C. W., Nanoparticle Size and Surface Chemistry Determine Serum Protein Adsorption and Macrophage Uptake. *Journal of the American Chemical Society* **2012,** *134*, 2139-2147.

23. Alric, C.; Miladi, I.; Kryza, D.; Taleb, J.; Lux, F.; Bazzi, R.; Billotey, C.; Janier, M.; Perriat, P.; Roux, S.; Tillement, O., The Biodistribution of Gold Nanoparticles Designed for Renal Clearance. *Nanoscale* **2013,** *5*, 5930-5939.

24. He, Y. P.; Miao, Y. M.; Li, C. R.; Wang, S. Q.; Cao, L.; Xie, S. S.; Yang, G. Z.; Zou, B. S.; Burda, C., Size and Structure Effect on Optical Transitions of Iron Oxide Nanocrystals. *Physical Review B* **2005,** *71*, 125411.

25. Tang, J.; Myers, M.; Bosnick, K. A.; Brus, L. E., Magnetite Fe3O4 Nanocrystals: Spectroscopic Observation of Aqueous Oxidation Kinetics. *The Journal of Physical Chemistry B* **2003,** *107*, 7501-7506.

26. Chen, A. L.; Hu, Y. S.; Jackson, M. A.; Lin, A. Y.; Young, J. K.; Langsner, R. J.; Drezek, R. A., Quantifying Spectral Changes Experienced by Plasmonic Nanoparticles in a Cellular Environment to Inform Biomedical Nanoparticle Design. *Nanoscale research letters* **2014,** *9*, 454.

27. Satiya, J.; Schwartz, I.; Tabibian, J. H.; Kumar, V.; Girotra, M., Ablative Therapies for Hepatic and Biliary Tumors: Endohepatology Coming of Age. *Translational gastroenterology and hepatology* **2020,** *5*, 15.

28. Alvarez-Sánchez, M. V.; Napoléon, B., Review of Endoscopic Radiofrequency in Biliopancreatic Tumours with Emphasis on Clinical Benefits, Controversies and Safety. *World J Gastroenterol* **2016,** *22*, 8257-8270.

29. Smith, M. A.; Houghton, P., A Proposal Regarding Reporting of *In Vitro* Testing Results. *Clinical Cancer Research* **2013,** *19*, 2828-2833.

30. Marangon, I.; Silva, A. A. K.; Guilbert, T.; Kolosnjaj-Tabi, J.; Marchiol, C.; Natkhunarajah, S.; Chamming's, F.; Ménard-Moyon, C.; Bianco, A.; Gennisson, J.-L.; Renault, G.; Gazeau, F., Tumor Stiffening, a Key Determinant of Tumor Progression, Is Reversed by Nanomaterial-Induced Photothermal Therapy. *Theranostics* **2017,** *7*, 329-343.

31. Eyerly, S. A.; Vejdani-Jahromi, M.; Dumont, D. M.; Trahey, G. E.; Wolf, P. D., The Evolution of Tissue Stiffness at Radiofrequency Ablation Sites During Lesion Formation and in the Peri-Ablation Period. *J Cardiovasc Electrophysiol* **2015,** *26*, 1009-1018.

32. Kwon, H.-J.; Kang, M.-J.; Cho, J.-H.; Oh, J.-Y.; Nam, K.-J.; Han, S.-Y.; Lee, S. W., Acoustic Radiation Force Impulse Elastography for Hepatocellular Carcinoma-Associated Radiofrequency Ablation. *World J Gastroenterol* **2011,** *17*, 1874-1878.

33. Levental, K. R.; Yu, H.; Kass, L.; Lakins, J. N.; Egeblad, M.; Erler, J. T.; Fong, S. F.; Csiszar, K.; Giaccia, A.; Weninger, W.; Yamauchi, M.; Gasser, D. L.; Weaver, V. M., Matrix Crosslinking Forces Tumor Progression by Enhancing Integrin Signaling. *Cell* **2009,** *139*, 891-906.

34. You, Y.; Zheng, Q.; Dong, Y.; Xie, X.; Wang, Y.; Wu, S.; Zhang, L.; Wang, Y.; Xue, T.; Wang, Z.; Chen, R.; Wang, Y.; Cui, J.; Ren, Z., Matrix Stiffness-Mediated Effects on Stemness Characteristics Occurring in HCC Cells. *Oncotarget* **2016,** *7*, 32221-32231.

35. Schrader, J.; Gordon-Walker, T. T.; Aucott, R. L.; van Deemter, M.; Quaas, A.; Walsh, S.; Benten, D.; Forbes, S. J.; Wells, R. G.; Iredale, J. P., Matrix Stiffness Modulates Proliferation, Chemotherapeutic Response, and Dormancy in Hepatocellular Carcinoma Cells. *Hepatology* **2011,** *53*, 1192-1205.

36. Sapareto, S. A.; Dewey, W. C., Thermal Dose Determination in Cancer Therapy. *International journal of radiation oncology, biology, physics* **1984,** *10*, 787-800.

37. Kolosnjaj-Tabi, J.; Di Corato, R.; Lartigue, L.; Marangon, I.; Guardia, P.; Silva, A. K.; Luciani, N.; Clement, O.; Flaud, P.; Singh, J. V.; Decuzzi, P.; Pellegrino, T.; Wilhelm, C.; Gazeau, F., Heat-generating Iron Oxide Nanocubes: Subtle "Destructurators" of theTumoral Microenvironment. *ACS Nano* **2014,** *8*, 4268-4283.

38. Ernsting, M. J.; Hoang, B.; Lohse, I.; Undzys, E.; Cao, P.; Do, T.; Gill, B.; Pintilie, M.; Hedley, D.; Li, S.-D., Targeting of Metastasis-Promoting Tumor-Associated Fibroblasts and Modulation of Pancreatic Tumor-Associated Stroma with a Carboxymethylcellulose-Docetaxel Nanoparticle. *J Control Release* **2015,** *206*, 122-130.

39. Zhang, J.; Miao, L.; Guo, S.; Zhang, Y.; Zhang, L.; Satterlee, A.; Kim, W. Y.; Huang, L., Synergistic Anti-Tumor Effects of Combined Gemcitabine and Cisplatin Nanoparticles in a Stroma-rich Bladder Carcinoma Model. *J Control Release* **2014,** *182*, 90-96.

40. Rice, A. J.; Cortes, E.; Lachowski, D.; Cheung, B. C. H.; Karim, S. A.; Morton, J. P.; Del Rio Hernandez, A., Matrix Stiffness Induces Epithelial-Mesenchymal Transition and Promotes Chemoresistance in Pancreatic Cancer Cells. *Oncogenesis* **2017,** *6*, e352.

41. Espinosa, A.; Di Corato, R.; Kolosnjaj-Tabi, J.; Flaud, P.; Pellegrino, T.; Wilhelm, C., Duality of Iron Oxide Nanoparticles in Cancer Therapy: Amplification of Heating Efficiency by Magnetic Hyperthermia and Photothermal Bimodal Treatment. *ACS Nano* **2016,** *10*, 2436-2446.

Graphical Abstract